Characterization of Higher Order Modes in the MAX IV Active 100 MHz Cavities

Jonas Björklund Svensson
jonas.bjorklund_svensson@maxlab.lu.se

Department of Electrical and Information Technology
Lund University

Advisor: Åke Andersson, Anders Karlsson

June 16, 2015

Printed in Sweden
E-huset, Lund, 2015

Abstract

In circular accelerators, and in storage rings in particular, charged particles are kept in a closed orbit for a very long time by means of a magnet lattice. When the particle beam is bent by the magnetic field it emits light, which decreases the particle beam energy by an amount equal to the radiated energy. Over many bends in the magnets and many turns in the machine, these relatively small energy losses amount to significant values, and so it is crucial to replenish this energy to keep the beam orbiting. In storage rings, such as the MAX IV rings, this is done with radio frequency (RF) cavities containing an oscillating electromagnetic field which, on average, restores the correct amount of energy each turn. However, the beam itself can excite so-called higher order modes (HOMs) in the cavities which can ruin the beam stability if these HOMs happen to resonate well and have certain resonating frequencies. The aim of this thesis is to determine the different HOMs of the active 100 MHz cavities of the MAX IV storage rings, as well as the impact these have on the beam stability.

Table of Contents

List of Figures

List of Tables

List of Acronyms

DBA Double-bend achromat

FEL Free-electron laser

FWHM Full width at half maximum

GeV Giga electron volt

HOM Higher order mode

IBC Impedance boundary condition

ID Insertion device

Linac Linear accelerator

MAX Microtron accelerator for X-rays

MBA Multi-bend achromat

PEC Perfect electric conductor

RAM Random-access memory

RF Radio frequency

SPF Short pulse facility

SR Synchrotron radiation

TE Transverse electric

TM Transverse magnetic

Chapter 1
Introduction

There is a higher demand than ever for synchrotron radiation, with reasearch groups from different scientific fields discovering its usefulness over the last decade [1]. The MAX IV synchrotron radiation facility, currently being built on the outskirts of Lund, Sweden, will provide scientists with light of higher quality[1] than any other currently existing light source [3].

In order to produce this light, electrons are accelerated through a full energy linear accelerator (linac) injector and are injected into one of the two storage rings or the short pulse facility (SPF). The larger storage ring will have a beam energy of 3 GeV and the smaller 1.5 GeV and they will be 528 m and 96 m in circumference, respectively [4, 5]. The light is "created" in insertion devices (IDs) called undulators and wigglers [3], by the basic principle that accelerated charged particles emit radiation, and is then carried through beamlines to the experiment stations.

The beam energy must be replenished to make up for the energy lost in the ID's and bending magnets in the form of light. Failure to do so leads to poor beam quality or even complete loss of the beam. To restore the energy, radio frequency (RF) cavities are most often used. These are placed at one or more locations around the storage ring and use resonating electromagnetic fields to accelerate the particles. The (active) RF cavities of the MAX IV rings use the fundamental resonance mode at 100 MHz to do this. Besides the active cavities, there are also passive harmonic cavities placed around the ring. These are used to elongate the electron bunches, which comprise the electron beam, and are fed by the beam itself, rather than an external power amplifier. Thus, the energy lost by the beam in those cavities has to be restored by the active cavities as well. The harmonic cavities have their fundamental mode around 300 MHz, the third harmonic of the active RF cavities [4, 5].

The electrons not only excite fields in the harmonic cavities, but also in the 100 MHz cavities. Of course, the field of the fundamental mode is excited, but also many higher order modes (HOMs) at higher frequencies than the fundamental frequency might be excited. If the amplitudes of the HOMs grow strong, they may affect the trajectories of the particles. In particular HOMs with frequencies close to critical beam frequencies, see Section 2.4, might give rise to an instability that destroys the beam quality or even kills the beam. Therefore, it is very useful to

[1] in terms of brilliance [2]

know how the frequencies of these HOMs change in relation to the fundamental mode when the cavity is tuned or when the temperature is changed due to deposited electromagnetic energy in the cavity walls. This thesis aims to determine the different HOMs of the active 100 MHz cavities of the MAX IV storage rings, as well as the impact these have on the beam stability, through measurements and evaluations of the HOMs and calculations of the instabilities.

The MAX IV facility

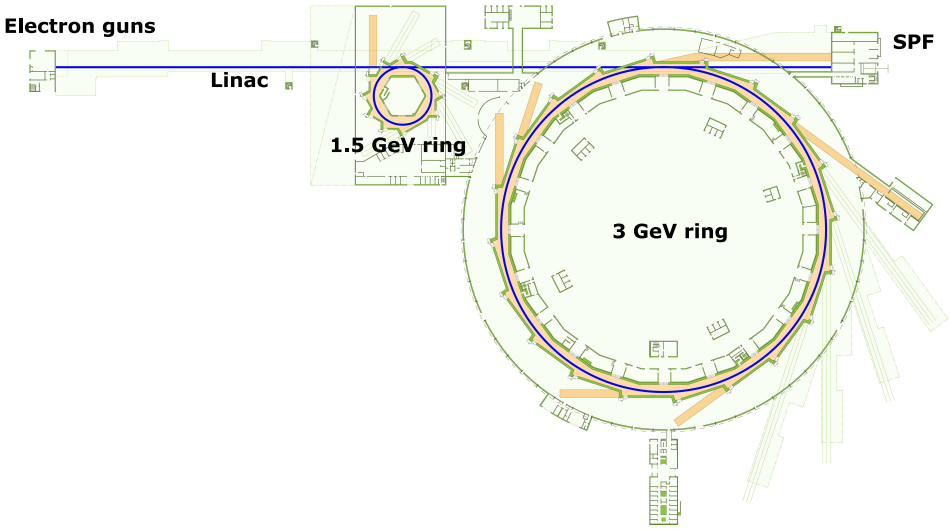

Figure 1.1: Overview of the MAX IV facility. Picture by Johnny Kvistholm.

The MAX IV facility consists of 4 main parts [4], not counting the X-ray beamlines, see Figure 1.1. The first part consists of the electron guns, one thermionic and one photocathode [6], and the linac which make up a full energy injector, i.e. a system where the energy of the electrons have nominal energy already at injection into the storage rings. This differs from e.g. MAX II, where the electrons are injected at a sub-nominal energy and then accelerated to full energy in the storage ring [7]. The second part is the smaller 1.5 GeV, 96 m circumference ring, which will provide the users with soft X-rays. This ring is energy- and size-wise similar to MAX II, but will of course be built with newer technology such as the new magnet block concept [8, 9].

The third part is the bigger 3 GeV, 528 m circumference, ring, which will provide the users with hard X-rays. This ring is one of the first of a new generation of storage rings [5], which will have very low emittance[2], and will be a big step towards diffraction limited light sources [5], i.e. where the X-ray spot size on the samples at the experiment stations will be limited by the optics and the diffraction

[2] a measure proportional to the electron beam size and divergence, [2, 10]

limit and not by the electron beam size. This is done by means of a multi-bend achromat[3] (MBA) lattice [5], whereas the 1.5 GeV ring will have a more common double-bend achromat[4] (DBA) lattice. The fourth part is the SPF, at the end of the linac. While the rings, because of the long bunch lengths, will produce fairly long light pulses, the SPF is, as its name suggests, designed specifically to produce short light pulses. There are also plans for extending the SPF into a free-electron laser (FEL) [2, 10]. [4]

Coordinate systems

In accelerator physics, it is very common to have a co-moving coordinate system with the coordinates x and z describing a deviation from the nominal orbit and the coordinate s describing the position around the machine [2]. There are not any equations that require a deeper knowledge of this type of system in this thesis, but it does appear in a few places and it is good to keep it in mind.

In electromagnetism, the coordinate system is often changed, or transformed, depending on the geometry of the studied system. The systems studied here, namely the RF cavities, have a high degree of axial symmetry, so therefore, we use a cylindrical coordinate system, see Figure 1.2. We do not derive the transformations to and from a cartesian coordinate system here; it is assumed that the reader has seen this type of coordinates before.

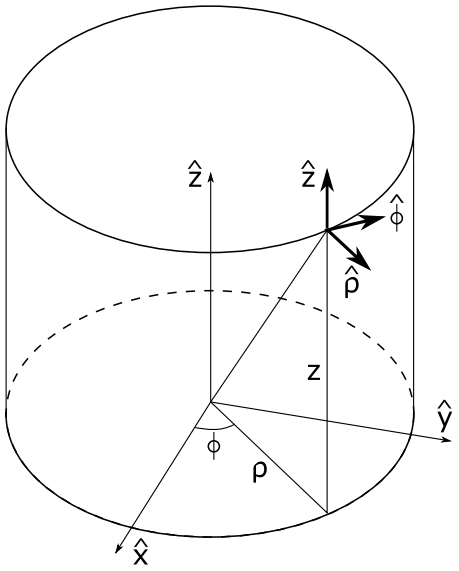

Figure 1.2: Schematic definition of the cylindrical coordinate system.

[3] Basically a symmetry section of the machine. There will be 20 of these achromats in the 3 GeV ring.

[4] 12 achromats in the 1.5 GeV ring.

Chapter 2
Theory

In this chapter the theoretical foundation of the thesis work is presented. We first describe resonance cavities in general and then focus on the MAX IV cavities. We then introduce the theoretically important entities Q-value and shunt resistance. Lastly, we look at the beam spectrum and the interaction between the cavity modes and the beam.

2.1 Resonance Cavities

Resonance cavities are hollow chambers made from some highly conductive material, usually copper when the cavity is used at room temperature or above. The cavity contains different modes which are highly dependent on the cavity geometry. These modes have certain distributions of the electromagnetic fields that can be excited in the cavity and the total field in the cavity can be decomposed into these modes. There is one field distribution and oscillating frequency for each mode. The mode with the lowest resonance frequency is called the fundamental mode and modes with higher frequency than this are called HOMs.

In the following section, we present some fundamental concepts in resonance cavity theory and the field equations for the modes in a cylindrical cavity with perfectly conducting walls.

2.1.1 Maxwell's equations

As with all macroscopic electromagnetic phenomena, the starting point of our study is Maxwell's equations:

$$\begin{aligned} \nabla \times \boldsymbol{E}(\boldsymbol{r},t) &= -\frac{\partial \boldsymbol{B}(\boldsymbol{r},t)}{\partial t} \\ \nabla \times \boldsymbol{H}(\boldsymbol{r},t) &= \frac{\partial \boldsymbol{D}(\boldsymbol{r},t)}{\partial t} + \boldsymbol{J}(\boldsymbol{r},t) \\ \nabla \cdot \boldsymbol{B}(\boldsymbol{r},t) &= 0 \\ \nabla \cdot \boldsymbol{D}(\boldsymbol{r},t) &= \rho(\boldsymbol{r},t), \end{aligned} \tag{2.1}$$

where $\boldsymbol{E}$, $\boldsymbol{B}$, $\boldsymbol{H}$, $\boldsymbol{D}$, $\boldsymbol{J}$ and ρ are the electric field, magnetic flux density, magnetic field, electric flux density, current density and charge density, respectively. For

simplicity, the first four vector fields are often called simply $\boldsymbol{E}$-field, $\boldsymbol{B}$-field, $\boldsymbol{H}$-field and $\boldsymbol{D}$-field. The two uppermost equations are often named Faraday's law of induction and Ampère's generalized law and the bottom equation Gauss' law. The corresponding boundary conditions at perfectly conducting surfaces are [11]:

$$\begin{cases} \hat{\boldsymbol{n}} \times \boldsymbol{E} = \boldsymbol{0} \\ \hat{\boldsymbol{n}} \times \boldsymbol{H} = \boldsymbol{J}_S \\ \hat{\boldsymbol{n}} \cdot \boldsymbol{B} = 0 \\ \hat{\boldsymbol{n}} \cdot \boldsymbol{D} = \rho_S, \end{cases} \tag{2.2}$$

where $\hat{\boldsymbol{n}}$ is the normal vector to the surface pointing into the enclosed volume, $\boldsymbol{J}_S$ is the surface current density and ρ_S is the surface charge density. At the frequencies relevant here (100-1500 MHz), copper is a very good conductor [12], so perfect electric conductor (PEC) boundary conditions is a reasonable approximation, as we shall see later. Since we have vacuum as a medium inside the cavities, we have the case where

$$\begin{cases} \boldsymbol{D} = \epsilon_0 \boldsymbol{E} \\ \boldsymbol{B} = \mu_0 \boldsymbol{H}, \end{cases} \tag{2.3}$$

where ϵ_0 is the vacuum electric permittivity and μ_0 is the vacuum magnetic permeability. With Eq. (2.3) the above equations can be expressed in terms of just two vector fields, often $\boldsymbol{E}$ and $\boldsymbol{H}$.

2.1.2 Solutions to Maxwell's equations

To obtain the (most practical) field equations for the cavities, one must make quite a few intermediate steps. These are left out here, but are thoroughly displayed in chapters 2, 4, 5 and 6 in [11]. We now show the solution for a cylindrical geometry with PEC boundary conditions. We let the z-axis be the symmetry axis, cf. Figure 1.2. Axially symmetric cavities are suitable since they have a mode with electric field in the z-direction and a maximum along the symmetry axis. The particles are then accelerated only in the z-direction. Often the diameter of the cylinder is of similar size to or greater than the length, and in such a case the cavity is usually referred to as a pillbox cavity.

The fields are time harmonic with time dependence $e^{-i\omega t}$, where ω is the angular frequency. We suppress the time dependence and use the complex space dependent fields. These are related to the time domain fields by

$$\boldsymbol{E}(\boldsymbol{r}, t) = \Re\left\{\boldsymbol{E}(\boldsymbol{r}, \omega) e^{-i\omega t}\right\},$$

where $\Re\{\}$ is the real part of the enclosed expression. The solutions are

$$\begin{cases} \boldsymbol{E}_{mn\ell}(\boldsymbol{r}) = \dfrac{k_{tmn}}{k_{mn\ell}} \sqrt{\dfrac{\varepsilon_\ell}{d}} \left(i \boldsymbol{E}_{Tmn}(\boldsymbol{\rho}) \sin \dfrac{\ell \pi z}{d} + \hat{\boldsymbol{z}} v_{mn}(\boldsymbol{\rho}) \cos \dfrac{\ell \pi z}{d} \right) \\ \boldsymbol{H}_{mn\ell}(\boldsymbol{r}) = \dfrac{k_{tmn}}{k_{mn\ell}} \sqrt{\dfrac{\varepsilon_\ell}{d}} \boldsymbol{H}_{Tmn}(\boldsymbol{\rho}) \cos \dfrac{\ell \pi z}{d} \end{cases} \tag{2.4}$$

for transverse magnetic (TM) modes with $\varepsilon_\ell = 2-\delta_{\ell,0}$, where $\delta_{i,j}$ is the Kronecker delta, and

$$\begin{cases} \boldsymbol{E}_{mn\ell}(\boldsymbol{r}) = i\dfrac{k_{tmn}}{\omega_{mn\ell}\mu_0}\sqrt{\dfrac{2}{d}}\boldsymbol{E}_{Tmn}(\boldsymbol{\rho})\sin\dfrac{\ell\pi z}{d} \\ \boldsymbol{H}_{mn\ell}(\boldsymbol{r}) = \dfrac{k_{tmn}}{\omega_{mn\ell}\mu_0}\sqrt{\dfrac{2}{d}}\left(\boldsymbol{H}_{Tmn}(\boldsymbol{\rho})\cos\dfrac{\ell\pi z}{d} + i\hat{\boldsymbol{z}}w_{mn}(\boldsymbol{\rho})\sin\dfrac{\ell\pi z}{d}\right) \end{cases} \tag{2.5}$$

for transverse electric (TE) modes. Indices t and T, for scalars and vectors, respectively, indicate transverse components, v_{mn} and w_{mn} are the (normalized) longitudinal components for the different mode types (TM/TE), d is the length of the cavity, $\boldsymbol{\rho} = (x, y)$ is the transverse coordinate and m, n, and ℓ are integer numbers with allowed values

$$m = 0, 1, 2, \ldots \quad n = 1, 2, 3, \ldots \quad \ell = \begin{cases} 0, 1, 2, \ldots & \text{TM} \\ 1, 2, 3, \ldots & \text{TE.} \end{cases}$$

$k_{mn\ell}$ and k_{tmn} are the total and transverse wavenumber of the modes, respectively.

The functions v_{mn} and w_{mn} are

$$v_{mn} = \frac{\sqrt{\varepsilon_m}J_m(\xi_{mn}\rho/a)}{\sqrt{\pi}aJ'_m(\xi_{mn})}\begin{pmatrix}\cos m\phi \\ \sin m\phi\end{pmatrix} \qquad k_{tmn}^2 = \frac{\xi_{mn}^2}{a^2} \tag{2.6}$$

$$w_{mn} = \frac{\sqrt{\varepsilon_m}\eta_{mn}J_m(\eta_{mn}\rho/a)}{\sqrt{\pi(\eta_{mn}^2 - m^2)}aJ_m(\eta_{mn})}\begin{pmatrix}\cos m\phi \\ \sin m\phi\end{pmatrix} \qquad k_{tmn}^2 = \frac{\eta_{mn}^2}{a^2}, \tag{2.7}$$

where a is the radius of the cavity, ξ_{mn} is the n^{th} zero to $J_m(\rho)$, η_{mn} is the n^{th} zero to $J'_m(\rho)$ and $J_m(\rho)$ is the cylindrical Bessel function of order m. ρ is the radial distance from the z-axis and ϕ is the azimuthal angle, and $\varepsilon_m = 2 - \delta_{m,0}$. Since we have perfect cylindrical geometry, the point $\phi = 0$ is arbitrary and so both the cosine and sine functions in Eqs. (2.6) and (2.7) can exist, which degenerates the modes with $m \neq 0$. The transverse components of the fields are obtained through

$$\begin{cases} \boldsymbol{E}_{Tmn}(\boldsymbol{\rho}) = \begin{cases} i\frac{k_{z\ell}}{k_{tmn}^2}\nabla_T v_{mn}(\boldsymbol{\rho}), & \text{TM} \\ -i\frac{\omega_{mn\ell}\mu_0}{k_{tmn}^2}\hat{\boldsymbol{z}}\times\nabla_T w_{mn}(\boldsymbol{\rho}), & \text{TE} \end{cases} \\ \boldsymbol{H}_{Tmn}(\boldsymbol{\rho}) = Z_{mn\ell}^{-1}\hat{\boldsymbol{z}}\times\boldsymbol{E}_{Tmn}(\boldsymbol{\rho}), \end{cases}$$

where $Z_{mn\ell}^{-1}$ is the mode impedance defined by

$$Z_{mn\ell} = \begin{cases} \frac{k_{z\ell}}{\omega_{mn\ell}\epsilon_0\epsilon_r}, & \text{TM} \\ \frac{\omega_{mn\ell}\mu_0}{k_{z\ell}}, & \text{TE,} \end{cases}$$

where $k_{z\ell} = \ell\pi/d$ is the longitudinal wavenumber and $k_{mn\ell}^2 = k_{tmn}^2 + k_{z\ell}^2$ and where ϵ_r is the relative electric permittivity. With these modes we have an associated resonance frequency, which is defined as

$$f_{mn\ell} = \frac{\omega_{mn\ell}}{2\pi} = \frac{k_{mn\ell}c}{2\pi} = \frac{c}{2\pi}\sqrt{k_{tmn}^2 + k_{z\ell}^2}, \tag{2.8}$$

Table 2.1: Frequencies for the 3 first TM and TE modes in a pillbox cavity. The radius is 1.148 m and the length is 0.376 m.

Mode	TM_{010}	TM_{110}	TM_{210}	TE_{111}	TE_{211}	TE_{011}
$f_{mn\ell}$ **[MHz]**	99.957	159.267	213.464	405.937	418.380	429.297

where c is the speed of light in the medium inside the cavity. The typical medium is vacuum, with the speed of light $c_0 = c\sqrt{\epsilon_r}$. It is here assumed, with good reason, that the medium is non-magnetic, and the relative permeability μ_r of the material has been left out throughout this section, since then $\mu_r = 1$. This is, in fact, valid for the whole cavity, since copper, used for the cavity walls, is only very slightly diamagnetic [13].

In reality, the time dependence of the fields is not purely harmonic, but also have a damping term because of resistive losses in the cavity walls. It can be shown that the total electric field, $\boldsymbol{E}(\boldsymbol{r}, t)$, can be expanded in terms of the solenoidal eigenfunctions, which are shown in Eqs. (2.4) and (2.5), together with a time dependent amplitude function [11],

$$\boldsymbol{E}(\boldsymbol{r}, t) = \sum_{n=0}^{\infty} e_n(t)\boldsymbol{E}_n(\boldsymbol{r}), \tag{2.9}$$

where $\boldsymbol{E}_n(\boldsymbol{r})$ are the solenoidal eigenfunctions and $e_n(t)$ are the time dependent amplitude functions. This leads to a differential equation in $e_n(t)$ which has the general solution

$$e_n(t) = A\cos(\omega t + \phi)e^{-\alpha_n t}, \tag{2.10}$$

where $\omega = \sqrt{\omega_n^2 - \alpha_n^2}$, ω_n is the resonance frequency and α_n is the attenuation constant of mode n. The time dependence is discussed more in Section 2.3.1.

2.1.3 Examples

As an example, we look briefly at the first few resonance frequencies in a pillbox cavity. One of them is be the $TM_{mn\ell} = TM_{010}$, which is the mode used for accelerating particles. The length of the pillbox is the same as for the MAX IV 100 MHz cavities, but the radius is much bigger to have the fundamental mode at the same frequency. This is discussed more in the next section.

Because η_{mn} can adopt a smallest value which is smaller than that of ξ_{mn}, see e.g. Appendix A in [11], the TE_{11} mode is the fundamental mode for an infinitely long cylindrical waveguide. However, now that we have a cylindrical cavity of finite length, this is not always true. In particular in this case, where we have a very flat pillbox shape, the lowest TE-mode, the TE_{111}, is far above the lowest TM-mode, the TM_{010}, see Table 2.1. Because of the flat geometry, there are very many TM HOMs with increasing m and n between the fundamental TM and TE modes.

The values in Table 2.1 were calculated analytically with Eq. (2.8). The software that was used for evaluating the modes shown in Figures 2.1 and 2.2 is a commercial software called COMSOL Multiphysics [14]. It was used extensively for

obtaining numerical results throughout this thesis. For this simple geometry, Eqs. (2.4) and (2.5) would give the exact solutions, but for more complex geometries, like the ones in the subsequent section, a numerical solver is necessary. Numerical calculations are never perfect, but the error in the frequencies obtained by Comsol was found to be less than 10 kHz.

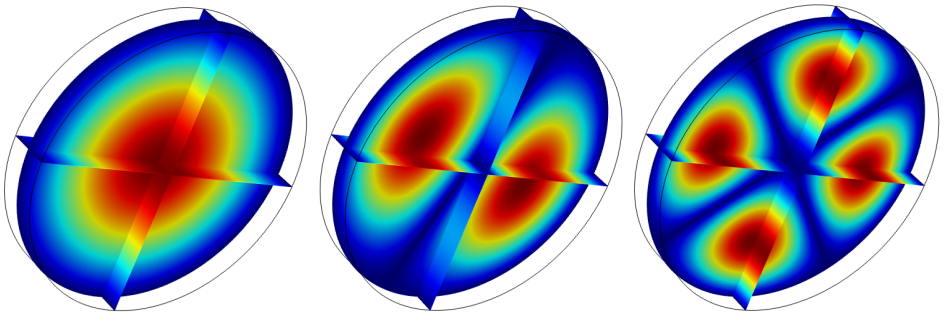

(a) TM_{010} **(b)** TM_{110} **(c)** TM_{210}

Figure 2.1: The electric field norm of the 3 lowest TM modes of a pillbox cavity.

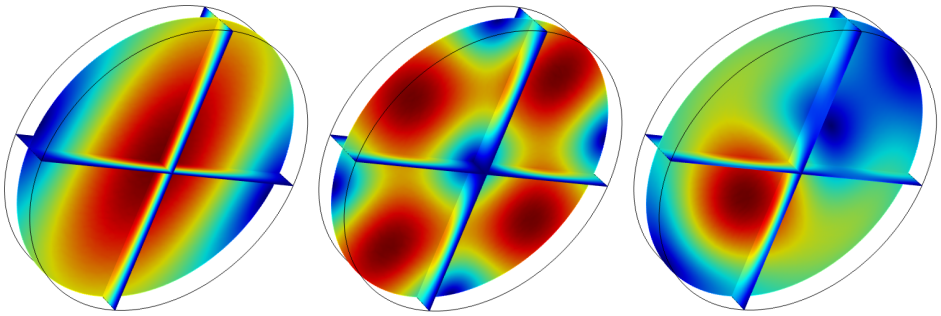

(a) TE_{111} **(b)** TE_{211} **(c)** TE_{011}

Figure 2.2: The electric field norm of the 3 lowest TE modes of a pillbox cavity.

The discrepancies arise because of the element sizes in the mesh, which, because of limited computer RAM, need to be fairly large. The memory usage is especially high for the 3D-solver, which was used here. However, while an axisymmetric 2D-solver would be able to find the mode in Figure 2.1a, and probably be more accurate, it would be more cumbersome to find the other modes in Figures 2.1 and 2.2, which have a non-constant ϕ-dependence. The 2D-solver can find these, but the index n has to be entered for each number. For a non-symmetric geometry, see Section 3.1, the 3D-solver is the only possibility, so therefore we decided to start by building, and evaluating, the simpler 3D geometries first.

2.2 The MAX IV Cavities

The cavities at MAX IV are of a type called capacity-loaded resonance cavitites, which, while differing quite a bit from the pillbox geometry, retain some of the same characteristics. There is still axial symmetry, but instead of having the end walls completely flat, there are so-called inner tubes with capacitance plates going into the cavity from one or both sides, see Figure 2.3. The electrons are accelerated by the electric field, or the electric potential, in the small gap in the left-most side of the Figure, along the z-axis.

The inner tubes and capacitance plates, internally in the MAX IV RF group called mushrooms for short (because of the apparent resemblance), introduce some of the characteristics of coaxial transmission lines into the pillbox. First, we only look at an axially symmetric model of the cavities and later move on to add more features like ports for power and HOM couplers.

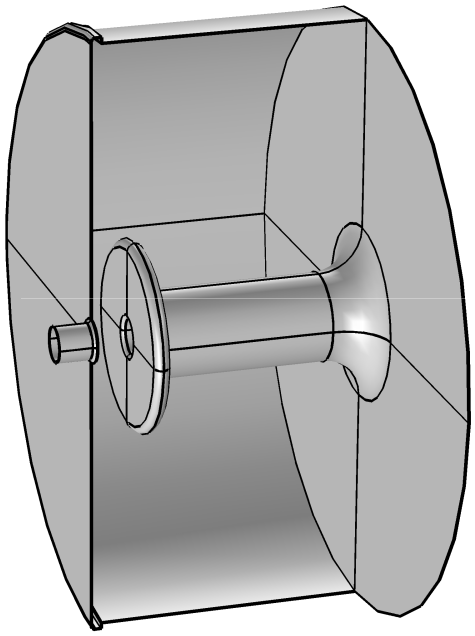

Figure 2.3: Internal shape of the 100 MHz cavities for MAX IV, without ports.

2.2.1 Features

One of the more noticeable effects of the mushroom(s) is that the spectral spacing between the fundamental mode and the first HOM is increased dramatically, somewhat like in a ridge waveguide. In fact, if one keeps the fundamental frequency the same, the radius of the cavity can be decreased from 1.148 m, in the pillbox case, to 0.410 m, in the 100 MHz cavities. At the same time, the first HOM is "pushed" upward, so that the bandwidth is also increased by a large amount. A

Table 2.2: Comparison of the frequencies of the first 6 modes in a pillbox and 100 MHz cavity, see Figure 2.3.

f_{pill} [MHz]	99.957	159.267	213.464	229.427	265.174	291.584
f_{100} [MHz]	99.962	409.199	419.590	461.315	470.988	531.739

good measure of this is the fractional bandwidth, defined as in Eq. (5.28) in [11]:

$$b_f = \frac{BW}{f_{center}} = 2\frac{f_1 - f_0}{f_1 + f_0},$$

where $BW = f_1 - f_0$ is the bandwidth and $f_{center} = \frac{1}{2}(f_1 + f_0)$ is the center frequency, with f_0 and f_1 being the frequency of the fundamental mode and first HOM, respectively. For the pillbox, $b_f = 0.458$, and for the 100 MHz cavity, $b_f = 1.215$. The fractional bandwidth is a more useful number for waveguides, but it serves well here as an example of how the frequencies are affected by the mushroom. See Table 2.2 for a quick comparison of the frequencies of the 6 first modes in either cavity.

The fundamental modes of the 100 MHz and harmonic cavities also look very different from the pillbox equivalent, cf. Figures 2.4 and 2.1a. Some HOMs, particularly the ones with very little field around the symmetry axis, look almost the same but also have their frequencies "pushed" upward, cf. Figures 2.5 and 2.1b. The fields of the fundamental modes are still axially symmetric and fairly confined to the center, but now the maximum does not occur on the z-axis, $\rho = 0$. Also, many modes are "switched around", i.e. they glide away from their original frequency if we continuously "grow" the mushroom out from one side of the pillbox, with a different amount for each mode. The first 3 HOMs in the 100 MHz cavity are completely different, as the first HOM, TM_{110}, in the pillbox gets pushed to the 4^{th} place in the 100 MHz cavity.

2.2.2 Fundamental modes

$\boldsymbol{E}$-field

Since the fundamental modes are of special interest for the acceleration of particles, we take a closer look at them. Figure 2.4 shows a cross section of the electric field norm of the fundamental mode of the 100 MHz cavities. The cross section is taken through the center of the cavity, cf. Figure 2.3. The frequency of this mode is 99.962[1] MHz, see Table 2.2. This mode is, as mentioned above, axially symmetric, which means that it looks the same no matter how we rotate the cavity around the z-axis. The z-axis is the symmetry axis of the cavity and it is thus the z-component of the electric field that accelerates the particles. However, because of the mushroom, the fundamental mode does not have a purely z-directed field

[1]While the fundamental frequency of the model is 99.962 MHz, the frequency that is used in the rings is 99.931 MHz. This is because we need an integer number of wavelengths around the ring to operate in a stable fashion. The cavity will be tuned to match this criterion as well as possible.

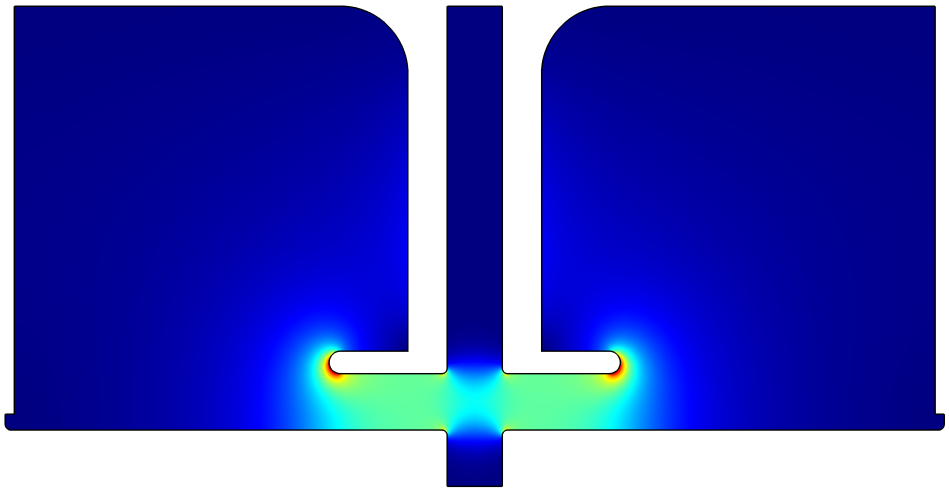

Figure 2.4: Cross section of the electric field norm of the fundamental mode in the 100 MHz cavities.

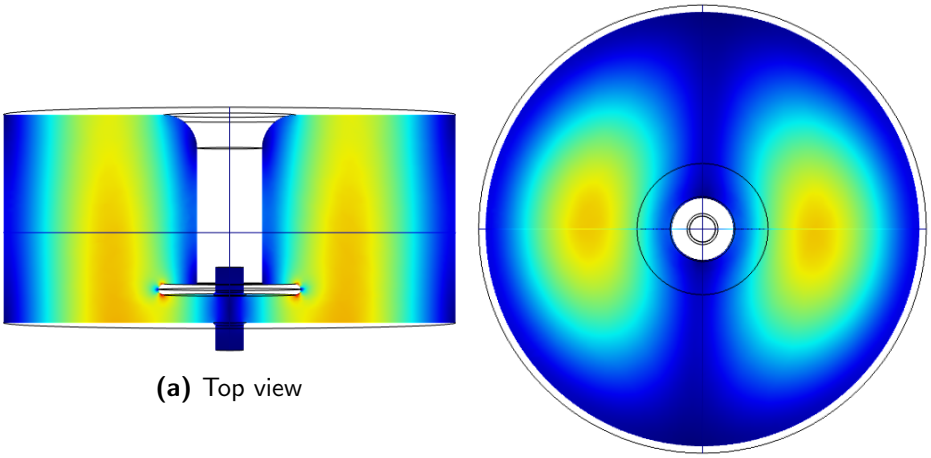

(a) Top view

(b) View along symmetry axis

Figure 2.5: Cross sections of the electric field norm of the 4$^{\text{th}}$ HOM at 470.985 MHz in the 100 MHz cavity

anymore, it also has ρ-component, see Figure 2.6. As seen in the figure, the z-component has the same sign along the z-axis, while the ρ-component changes sign. Please note that the color scale has changed since we now also have negative values; while $|\boldsymbol{E}| = 0$ was dark blue before, it is now green. However, only electrons outside the axis experience the ρ-components, since it vanishes on axis, and because of the change in sign, the total, integrated ρ-field experienced by the electrons should be small.

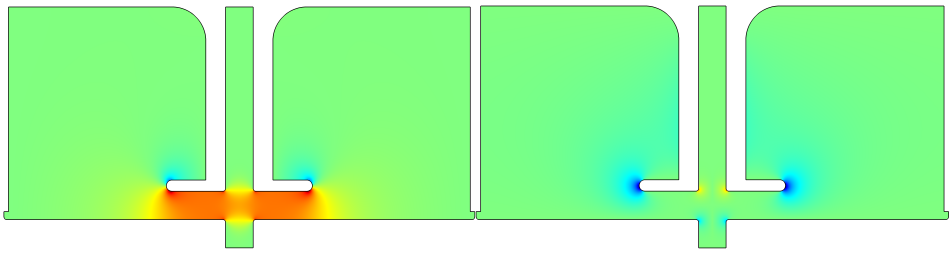

(a) z-component **(b)** ρ-component

Figure 2.6: Components of the $\boldsymbol{E}$-field of the fundamental mode in the 100 MHz cavities. Please note the difference in color scale from the norm plots.

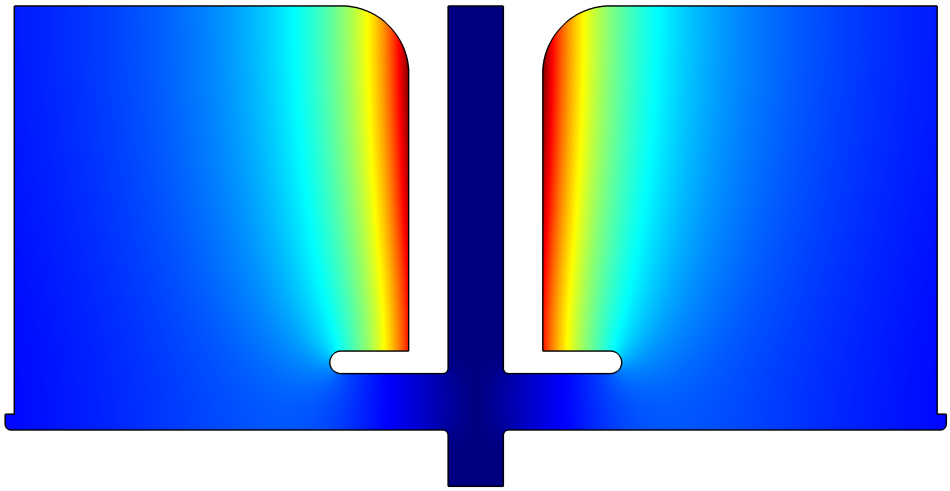

Figure 2.7: Cross section of the $\boldsymbol{B}$-field norm of the fundamental mode in the 100 MHz cavities.

$\boldsymbol{B}$-field

So far, we have only looked at the $\boldsymbol{E}$-field; now, we investigate also the $\boldsymbol{B}$-field. Although this field has no direct implications for the calculations presented in this thesis, see Section 2.4, it has some practical implications with regards to cavity design. One important use of the $\boldsymbol{B}$-field is for coupling the power from the transmission line to the fundamental mode in the cavity. This is done via a coupling loop, see Figure 3.7, which is placed in the ρ-z-plane, since the $\boldsymbol{B}$-field of the fundamental mode only has a ϕ-component.

As can be seen in Figure 2.7, the field is strongest along the inner tube, and therefore the surface current density, $\boldsymbol{J}_S$, also takes on its largest values in the same areas, see Eq. 2.2. Because of this, and that the walls are not actually perfectly conducting, extensive watercooling of the mushroom is necessary. Since the $\boldsymbol{B}$-field of the fundamental mode only has a ϕ-component, the surface currents

from this mode run from the capacitance plate, along the inner tube and around the cavity to the "bottom" side in Figure 2.7.

2.3 Circuit analogy, Q-value and shunt resistance

In this section of the chapter, we look shortly at some other important aspects, namely the circuit equivalent of a cavity, the Q-value of a mode and the thereto related shunt resistance. These are important measures, because they tell us about how well a mode resonates in the cavity and how strong the resulting field is in the beam region.

2.3.1 Circuit analogy

To simplify the understanding of some characteristics of resonance cavities, one can make a RLC circuit equivalent of the cavity, consisting of a capacitance, C, an inductance, L, and a shunt resistance (or equivalent resistance), R_{sh} [11, 15]. Many types of resonance circuits exist, but here we choose a parallel circuit. The capacitance and inductance together form the actual resonance circuit, while the shunt resistance accounts for the resistive losses in the cavity walls. For each mode we have a unique value of R_{sh}, L and C, with which the resonance frequency and attenuation constant of the circuit can be calculated from e.g. Eq. (6.7) in [11]. The solution to this equation is

$$v(t) = A\cos(\omega t + \phi)e^{-\alpha t}, \tag{2.11}$$

where $v(t)$ is the voltage over the circuit components, $\omega_0 = 1/\sqrt{LC}$ is the resonance angular frequency, $\alpha = 1/(2R_{sh}C)$ is the attenuation constant and $\omega = \sqrt{\omega_0^2 - \alpha^2}$. Modes that resonate well in the circuit have high values of R_{sh} and C, since a high resistance in a parallel RLC circuit makes most of the current go through the capacitance and inductance, which are inherently lossless.

In fact, the time dependent amplitude function, $e_n(t)$ (see Eq. (2.10)), for the electric field in the cavity satisfies the same equation as the voltage in the circuit equivalent, and thus has the same time dependence. This means that circuit theory helps us evaluate the time dependence of the electric fields in a resonance cavity.

2.3.2 Q-value and shunt resistance

The Q-value, or Quality factor, is a measure of the attenuation of a mode. The Q-value of a mode is defined by [11, 15]

$$Q = 2\pi \frac{\text{stored energy time averaged over one period}}{\text{dissipated energy during one period}} = 2\pi f \frac{W}{P_{loss}}, \tag{2.12}$$

where P_{loss} is the dissipated energy per period for the given mode. For example, a mode might have one of the previously mentioned "dangerous" resonance frequencies, but if the Q-value is low, i.e. if the mode does not resonate for very long

in the cavity, it might not affect the beam very much. There are different ways to quantify this, but the one used here is [11]

$$Q = \frac{f_0}{\Delta f} = \frac{f_0}{f_+ - f_-}, \tag{2.13}$$

where f_0 is the peak frequency of a mode and f_+ and f_- are the frequencies at either side of the peak at -3 dB from the peak amplitude (full width at half maximum, FWHM). This quantization originates from circuit theory and is applicable since we can make an accurate circuit equivalent of the cavity. The -3 dB limit for FWHM is valid when speaking in terms of power amplitudes, not voltage.

It is not a big surprise then, that the Q-value and the attenuation coefficient, α, are connected [11, 15]:

$$Q = \frac{\omega_0}{2\alpha} = \omega_0 R_{sh} C = \frac{R_{sh}}{\omega_0 L}. \tag{2.14}$$

Thus, by measuring the Q-value, we can obtain information on for how long a mode resonates in the cavity via Eq. (2.11). However, it is difficult to measure the capacitance and inductance, so one must often rely on a theoretical calculation of the shunt resistance, which can then be corrected to better correspond to the real case, see below. While α gives the decay time of the fields, the shunt resistance is used in many applications, e.g. the software ZAP, see Section 3.3, since it is in fact important for the total force on the beam, and thus influences instabilities [10]. The shunt resistance can be defined as [11]

$$R_{sh} = \frac{V^2}{P_{loss}}, \tag{2.15}$$

where V is the voltage over the path which the electrons take, i.e. roughly the symmetry axis, z. The voltage between two points is defined as the line integral of the electric field between these two points,

$$V = \int_{axis} \boldsymbol{E} \cdot d\boldsymbol{s} = \int_{axis} E_z(0,0,z)dz.$$

While the path integrated over corresponds quite well with the real path the electrons take, the actual field strength might not. As seen in Eq. (2.10), the electric field of the different modes varies as a $\cos(\omega t)$. We here omit the extra phase constant ϕ, since we cannot say at which phase in any given mode the bunch enters the cavity. We also omit the decay factor, since the transit time, the time it takes the bunch to pass the accelerating gap, is likely short compared to the decay time, and that a non-decaying mode is the worst-case we can observe.

Multiplying by $\cos(\omega t)$ (with $t = z/c$; $z = 0$ in the middle of the gap) gives us the transit time corrected voltage, which leads to the corresponding transit time corrected shunt resistance

$$V_{corr} = \int_{axis} E_z \cos(\omega \frac{z}{c})dz. \tag{2.16}$$

Although this does not give us the exact value of the voltage for each mode, due to the unknown initial phase, it gives us information about which modes have a very low shunt resistance in reality, and thus which modes we can disregard in our later analysis. These modes are modes with an angular frequency such that the transit time of the bunch is close to a full period of the mode, which then leads to a very small net voltage. For the other modes, we should obtain the highest possible values, so that we can later analyze a worst-case scenario.

The power loss is dependent on the surface current density and the conductive properties of the cavity material:

$$P_{loss} = \frac{R_S}{2} \iint_S |\boldsymbol{J}_S|^2 dS, \tag{2.17}$$

where $R_S = \sqrt{\frac{\omega\mu_0}{2\sigma_c}}$ is the surface resistance and σ_c is the surface conductivity. Both types of line integrals shown above can be evaluated numerically in Comsol once the field distribution has been determined. It is also fairly straightforward to write custom expressions containing the different factors.

Since the actual shunt resistance was not measured, another method was used to estimate it. It is known that the fraction R/Q is independent of cavity wall conductivity, and only dependent on the actual mode and the general geometry [15], since, from Eq. (2.14),

$$\frac{R_{sh}}{Q} = \frac{1}{\omega_0 C} = \omega_0 L = \sqrt{\frac{L}{C}}.$$

This means that this fraction should be more or less the same for the theoretical and measured values, since there are only very minor differences in geometry that might affect L and C. Thus, we use the relation

$$\frac{R_{meas}}{Q_{meas}} = \frac{R_{sim}}{Q_{sim}} \quad \Leftrightarrow \quad R_{meas} = \frac{Q_{meas}}{Q_{sim}} R_{sim} \tag{2.18}$$

to get an estimation of the actual value for the shunt resistance. For the first few modes, $R_{meas} \approx R_{sim}$, but as we go to the higher HOMs, the theoretical model is less and less accurate because of the large mesh, but also because some features, like the pump slots and surface roughness, are not in the model. The relations in Eq. (2.18) should still hold true, though.

2.4 Interaction with the beam

While the $\boldsymbol{E}$-field can accelerate the particles, the $\boldsymbol{B}$-field cannot change their energy at all [16]. However, it can bend, or "kick", their trajectory and can therefore also drive oscillations in the electron path around the ring. Thus, the HOMs can accelerate and/or kick the beam in a uncontrolled way. The magnitude of either of these effects is of course dependent on the field strength at the time of passage of the electron bunches, which itself is dependent on the amplitude, phase and the spatial distribution of the fields, see Eqs. (2.9) and (2.10). If some of

the bunches are in phase with the field of a HOM, like for the fundamental mode, they encounter the same field every time they pass through the cavity. This causes the effect of the mode on the beam, and also the amplitude of the mode itself, to increase at every passage. This is but one source of instabilities. In this thesis, the focus is on longitudinal effects, which means that we only take the influence of the E_z-component into account through the shunt resistance.

These effects can, of course, only arise if there are any such modes present in the cavities. Because of the fractional bandwidth being so high for the 100 MHz cavity (see Section 2.2.1), there is really no chance of the power source, which is spectrally quite pure, inducing any HOMs in the cavities; all HOMs are excited by the beam itself. If the bunches were infinitely short or had infinitely sharp edges, a Fourier analysis would show that they contained infiniely high frequencies. This is not the case, since the bunches in MAX IV are designed to be longitudinally extended[2] and shaped, ideally, like a quartic Gaussian, e^{-ks^4}, where s is the longitudinal coordinate. Thus, the beam only excites a certain, finite spectrum of frequencies and it is only if the cavity has a mode near one of these frequencies that it can grow to a considerable strength. The mode also needs to have some non-zero z-component of the electric field in the beam region, otherwise it is not excited to begin with[3], but this is included when calculating the shunt resistance.

2.4.1 Synchrotron oscillation

The energy gain of a charged particle traversing a voltage is $E = qU$, where $q = e$ is the elementary charge. If we look at the main accelerating voltage in the cavity, from the fundamental mode, it has the sinusoidal shape $U = U_{max}\sin(\Psi)$, c.f. Eq. 2.11, see Figure 2.8. One point in phase, Ψ_0, corresponds to the phase at which a nominal particle would arrive and gain exactly the amount of energy lost around the orbit [2]. Note, however, that far from all particles are nominal and that some particles in a bunch arrive later, Ψ_1, and earlier, Ψ_2, and gain different amounts of energy.

Because the electrons are very light, they become relativistic very quickly. This means that although they might gain or lose a little bit of extra energy, there is no noticeable change in velocity. We do however have the relation $R = mv/eB$, where R is the particle trajectory bending radius, $m = m_0\gamma$ is the particle mass with m_0 being the rest mass and γ being the relativistic factor, v is the particle velocity and $B = |\boldsymbol{B}|$ [2]. We see from this that even though we essentially have $v = c =$ constant, the relativistic mass of the particle still changes with γ and thus the bending radius also changes. Larger bending radius for larger energies, and vice versa, translates to a longer path length around the machine for higher energy particles than for lower energy particles.

Because we have no change in velocity, this change in path length translates into a change in arrival time and thus a change in RF phase, Ψ. A higher energy particle takes a longer path, taking longer time, and thus arrive later, see Ψ_1 in Figure 2.8, and vice versa for a lower energy particle, Ψ_2. This means that a higher

[2] An effect of the harmonic cavities

[3] And it would, conversely, not affect the beam if it had been excited by some other means

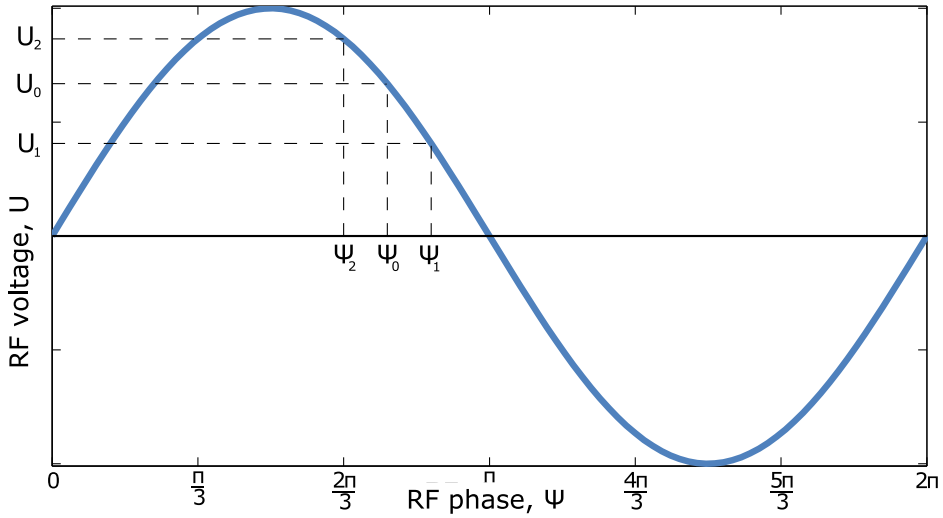

Figure 2.8: Particles arriving at different RF phase. These gain different amounts of energy, and because of difference in path length, they approach the nominal phase, Ψ_0.

energy particle gains less than nominal energy, $E_0 = eU_0$, which means that over one turn, the net effect is a loss of energy. Conversely, a lower energy particle has a net gain of energy. Thus, the particles slowly start to approach the nominal phase, overshoot it and start the procedure over. These oscillations around the nominal phase are called synchrotron oscillation, with angular frequency ω_s. Even though we have talked about this for individual particles, it also translates to motion of the whole bunch, which, in the lowest order approximation, can be seen as a macroparticle. This macroparticle oscillation is studied further in Subsections 2.4.2 and 2.4.3 and is a quite good approximation.

The voltage in Figure 2.8 gives rise to a potential in Ψ with a minimum around Ψ_0, which for small oscillations is linear and similar to a harmonic oscillator with eigenfrequency ω_s. Larger oscillations experience a more non-linear potential and even larger oscillations can fall out of the potential well altogether. How much the energy and phase can deviate from the nominal values is dictated by the so called separatrix, which encloses a stable region in the ΔE-$\Delta\Psi$ phase space. This stable region is called a bucket. [2] There are many such buckets around the ring that can be filled with particles. The buckets can be filled in different ways and the way the buckets are filled is called the filling pattern. The filling pattern affects the beam spectrum, see Subsection 2.4.2, and for a light source, this also affects the outgoing light in the beamlines.

2.4.2 Beam spectrum

To calculate the spectrum of the beam, one can take the Fourier transformation[4] of the beam current, $j(t)$, sampled at one spatial point in the ring, see e.g. [17],

$$J(\omega) = \int_{-\infty}^{\infty} j(t) e^{-i\omega t} dt,$$

$$j(t) = \frac{1}{2\pi} \int_{-\infty}^{\infty} J(\omega) e^{i\omega t} d\omega.$$

The temporal distribution of the current looks somewhat like a picket fence made out of peaks shaped like the individual bunches, see Figure 2.9a. The peaks will, if all buckets are filled, be spaced with roughly the RF period, T_{RF}, and the filling pattern repeats itself after the revolution period, T_0. The resulting spectrum can be seen in Figure 2.9b. The small peaks, revolution peaks, stem from the revolution period and the differences in bunch charge. The properties of the Fourier transform makes the envelope of the spectrum take the shape of the bunches, so that we do not have an infinite spectrum. The wider the bunches, the more narrow the spectrum.

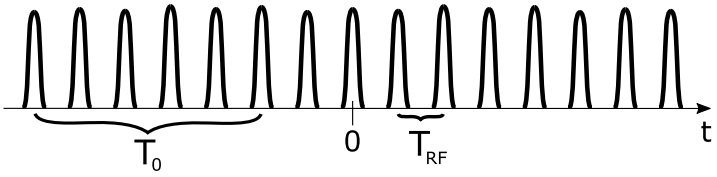

(a) Current signal in time.

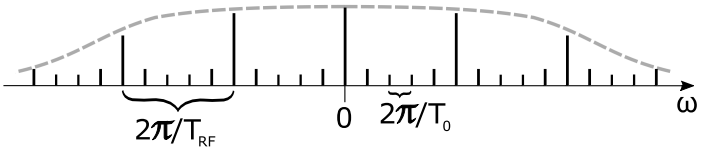

(b) Resulting ferquency spectrum.

Figure 2.9: The beam current function sampled at one spatial point in the ring and the resulting spectrum.

The bunches also oscillate around the nominal RF phase with the relatively slow synchrotron frequency, ω_s [2], see Subsection 2.4.1. There are more effects which contribute to the total spectrum, such as transverse oscillations, charge variation between bunches and oscillations within the bunches themselves, but these are neglected here. As an example to better show the effects of these synchrotron oscillations, we can look at the case where we have one pointlike bunch going around the ring, with small, rigid synchrotron oscillations around the nominal

[4]Please note that the timing convention here is different from that in Subsection 2.1.2.

phase [17]:

$$j_1(t) = \sum_{n=-\infty}^{\infty} \delta(t - nT_0 - \tau\cos[\omega_s nT_0]),$$

where τ is some small amplitude in time of the oscillations. The Fourier transform of this is

$$\begin{aligned} J_1(\omega) = \sum_{k=-\infty}^{\infty} e^{-i\omega(kT_0 - \tau\cos[\omega_s kT_0])} \approx \\ \approx \omega_0 \sum_{k=-\infty}^{\infty} \Big[\delta(\omega - k\omega_0) - \frac{i\tau}{2}(k\omega_0 - \omega_s)\delta(\omega - k\omega_0 + \omega_s) \\ - \frac{i\tau}{2}(k\omega_0 + \omega_s)\delta(\omega - k\omega_0 - \omega_s)\Big], \end{aligned} \tag{2.19}$$

where $\omega_0 = \frac{2\pi}{T_0}$ is the revolution angular frequency. The approximation lies in the small amplitude, τ. We see from Eq. (2.19) that the spectrum has main peaks at integer values of the revolution frequency, $k\omega_0$, with sidebands at $k\omega_0 \pm \omega_s$. Adding more terms to the approximation, which is needed if the oscillations are larger, adds more sidebands. When all $h = \frac{T_0}{T_{RF}}$ buckets are filled, as in Figure 2.9a, the synchrotron oscillations of the different bunches couple through the HOMs they give rise to. We then have h so-called longitudinal coupled bunch modes in the beam, instead of just the single synchrotron oscillation we saw above. The result of this is peaks at $k\omega_{RF}$, with sidebands at $k\omega_{RF} \pm (\mu\omega_0 + \omega_s)$, where $\mu = 0, ..., h-1$ is an integer index of the different longitudinal coupled bunc modes. We see that the index μ factors to the ω_0 term. This is because the difference in phase, due to different longitudinal coupled bunch modes, between the bunches cause their revolution angular frequency to shift a bit, but their synchrotron frequency is unaffected.

2.4.3 Instabilities

A few times in this text we have mentioned instabilities, which are oscillations of the beam itself around its nominal orbit and phase, driven by e.g. the HOMs, which can grow so large that the beam is lost. There are both longitudinal and transverse instabilities, both for subsequent bunches (collective instabilities) and even within the bunches. The E_z component of the HOMs has a great impact in the longitudinal direction[5]. We can see from e.g. Table A.1 that most of the modes are TM modes, which means that the E_Z-component, for symmetry reasons, is the only non-zero $\boldsymbol{E}$-field component on axis. From the same table we can also see which modes can have a net accelerating effect on the particles in the longitudinal direction by looking at the shunt resistances.

[5]Please note, though, that many TM-modes also have a quite large $\boldsymbol{B}$-field amplitude in the beam region, which can have a considerable effect on the beam in terms of transverse coupled bunch instabilities. This is one example of future work that is needed, see Chapter 6.

From Eqs. (2.11) and (2.14), we can see that the time for the amplitude of a mode to decrease to half of its maximum value is

$$t = \frac{\ln 2}{\pi} \frac{Q}{f_0}.$$

This gives us times on the order of some tens of μs, which can be compared to the temporal spacing of the bunches of 10^{-8} s, if every bucket is filled. Thus we can conclude that the fields remain in the cavity for much longer than it takes for a new bunch to enter, so that the HOM fields from a bunch affect a large number of the following bunches.

The synchrotron oscillations described in Subsection 2.4.1 have many modes, the first of which is the dipole mode, a rigid translation of the whole bunch, labeled with the index $a = 1$. We here limit ourselves to this the most basic case, and neglect the more complex higher order modes, i.e. quadrupole, $a = 2$, sextupole, $a = 3$, etc. With this established, we now know that the instabilities we study here are the rigid longitudinal coupled bunch instabilities.

Calculating the mode growth times

The HOMs can act as a driving force which make the synchrotron oscillations grow in size until the bunches, or part of them, eventually "fall out" of the bucket. To find out how dangerous such a mode is, one can calculate the complex coherent synchrotron frequency shift, which in the Sacherer-Zotter formalism has the form [18]

$$\Delta\omega^{\parallel}_{\mu,a} = i \left(\frac{a}{a+1} \right) \frac{e I_b \omega_0^2 \eta}{3 \left(\frac{L}{2\pi R} \right)^3 E \beta^2 2\pi\omega_s} \cdot \left[\frac{Z^{\parallel}}{n} \right]^{eff}_{\mu,a}. \tag{2.20}$$

Here, $\mu = 0, 1, ..., h-1$ is the integer index for the different longitudinal coupled bunch modes (see Subsection 2.4.2), $a = 1, 2, ...$ is an integer index for the synchrotron oscillation modes of the individual bunches and the superscript $\parallel$ indicates that it is the longitudinal quantities we study. I_b is the average bunch current, η is the momentum compaction factor (see e.g. [2,10]), $L = 2\sqrt{\pi}\sigma_\ell$ is the bunch length (with σ_ℓ being the standard deviation of the Gaussian bunch shape), R is the average radius of the ring, E is the beam energy, $\beta = v/c \approx 1$ and

$$\left[\frac{Z^{\parallel}}{n} \right]^{eff}_{\mu,a} = \frac{\sum_{k=-\infty}^{\infty} Z^{\parallel}(\omega_k^{\parallel}) \omega_0 \omega_k^{\parallel -1} h_a(\omega_k^{\parallel})}{\sum_{k=-\infty}^{\infty} h_a(\omega_k^{\parallel})},$$

where $Z^{\parallel}(\omega_k^{\parallel})$ is the longitudinal impedance, $\omega_k^{\parallel} = (kh + \mu + a\nu_s)\omega_0 = k\omega_{RF} + \mu\omega_0 + a\omega_s$ (cf. Subsection 2.4.2 with $a = 1$) and $h_a(\omega_k^{\parallel})$ is a frequency dependent form factor of the synchrotron mode, a, which is dependent on the unperturbed bunch shape and length. $Z^{\parallel}(\omega)$ has the equation [18]

$$Z^{\parallel}(\omega) = \frac{R_{sh}}{\left(1 + iQ \left(\frac{\omega_r}{\omega} - \frac{\omega}{\omega_r} \right) \right)},$$

where ω_r is a cavity resonance angular frequency. $h_a(\omega)$ has, for gaussian bunches, the equation [18]

$$h_a(\omega) = \left(\frac{\omega\sigma_\ell}{\beta c}\right)^{2a} exp\left[-\left(\frac{\omega\sigma_\ell}{\beta c}\right)^2\right].$$

The HOM spectrum that one compares to is the one of the cavity being examined. $Z^{\parallel}(\omega_k^{\parallel})$ is very small for most frequencies, but if the beam has a frequency near or on one of the HOMs, this entity can grow from zero to R_{sh}.

The frequency shift in Eq. 2.20 is, as mentioned, complex, which means that it has a real and an imaginary party. The real part, $\Re\{\Delta\omega_{\mu,a}^{\parallel}\}$, turns out to be the real coherent synchrotron angular frequency shift of a mode, while the imaginary part gives the growth rate of the mode, $\Im\{\Delta\omega_{\mu,a}^{\parallel}\} = r_{gr} = \frac{1}{\tau_{gr}}$, with τ_{gr} being the growth time.

Synchrotron radiation damping

Luckily, there are not only growth effects, but also damping effects which can cancel out and have an overall damping effect on the oscillations. The most obvious of these, at least for a light source, is the damping due to synchrotron radiation (SR). SR is always created when changing the velocity vector of a charged particle, which is done in the many magnets around the storage ring. This damping rate has the expression [2]

$$a_s = \frac{W_0}{2T_0E}(2 + \mathcal{D}),$$

where W_0 is the radiated energy during one turn of a particle travelling along the nominal orbit and $\mathcal{D}$ is a term from particles not travelling along the nominal orbit and which is set by the magnet lattice. The value of W_0 and $\mathcal{D}$ for the MAX IV 3 GeV ring are 360 keV and -0.847, respectively [2, 19], which gives us a damping time of $1/a_s \approx 0.0252$ s = 25.2 ms. A quick note should be made here: these values are for a "bare", linear lattice, i.e. a lattice where only the guiding and focusing elements, dipole and quadrupole magnets, are taken into account. Since the majority of the light is produced in the IDs, these also contribute to the damping rate[6]. When comparing to the growth times, we want the case with the least possible SR damping, which is without IDs.

Landau damping

There is also another source of damping, which stems from the RF system itself. We said above that the potential experienced by the particles was similar to that of a harmonic oscillator; this is not true when we have a double RF system, i.e. one type of cavity with a fundamental frequency and another type with some multiple of this frequency, like the active 100 MHz cavities and the passive 300 MHz harmonic cavities. Having a system like this creates a flattening of the potential around Ψ_0 that not only enables bunch lengthening, but also introduces so-called Landau damping of the synchrotron oscillations because of the non-linear forces

[6]There may even be special damping wigglers installed in the machine, see [3].

around the nominal phase. With a single RF system we have more or less only one synchrotron frequency, ω_s, for small oscillations, but with a double RF system, we get a broadening of this frequency by $\Delta\omega_s \approx 1022$ Hz. [20] This means that we now have particles with a narrow band of synchrotron frequencies, and as we know from basic mechanics, the oscillation amplitude of a driven oscillator declines as we go away from the resonance frequency, which in our case is ω_s. Thus, instabilities may start to grow, but when they have grown enough in amplitude, the synchrotron frequency of the particles starts to spread and they "slide off" the resonance [10]. The Landau damping time is given by approximately $1/(0.6\Delta\omega_s) \approx 1.6$ ms [21].

Course of action

It is crucial to calculate growth times for the instabilities, see Section 3.3, and compare them with the damping times. The end result is not some kind of equilibrium between the different effects; it is rather the case that one effect takes over, in the sense that if the damping time is shorter than the instability growth time, the total effect is damping. Since there are $h = 176$ coupled bunch modes in the MAX IV 3 GeV ring, the growth times of all of these modes must be calculated and compared to the different damping times.

Chapter 3

Theoretical work and Measurements

This chapter describes numerical calculations, using Comsol and ZAP, and measurements.

3.1 Numerical calculations using 3D models

The cavity shape that has been used previously, e.g. in Figure 2.3, is a simplification of the real cavities. In reality, there are also ports for pumps, needed to obtain and maintain a high vacuum, HOM dampeners and power couplers, see Figure 3.1. In the model, only the ports for power and HOM couplers have been included, since they have a simple, cylindrical shape. The coupling loops themselves are not included, the models have a "blind flange" instead. The pump ports have been left out since they, unlike the power and HOM ports, which are open and circularly shaped internally, are slotted, which means that the hole shape is a set of oblong slots of varying lengths. This was too difficult and/or time demanding to model, so they were excluded. This turned out to affect the precision of some modes in the model, most likely the ones with a surface current density not parallel to the slots. Apart from this, also the probe loop ports, placed on the end of the cavity towards the bottom of the "mushroom", were left out, since their influence is negligible.

The effect of the extra ports on the previously symmetric geometry is that we introduce new field components around the edges of the ports, e.g. a ϕ-component where there were previously only ρ- and z-components, so that we no longer have pure TE- or TM-modes. The volume also increases a bit, so the resonance frequencies of most modes decrease. Besides this, also the Q-values and shunt resistances change, most likely due to the surface currents having to re-route. The results from the extended 3D geometry evaluation are collected in Table A.1 in Appendix A Subsection A.1.1. In this table we list the obtained resonance frequencies, Q-values according to Eq. (2.12), shunt resistance according to Eq. (2.15) and (2.16) and finally the corrected shunt resistance according to Eq. (2.18).

It was previously also assumed that the boundary was a perfect electric conductor, which is obviously not completely realistic. In Comsol, there is an option to run the computation with the impedance boundary condition (IBC), where the material parameters for the boundary, here copper, and the frequency dependence are taken into account. Evaluations in Comsol's axisymmetric solver showed that

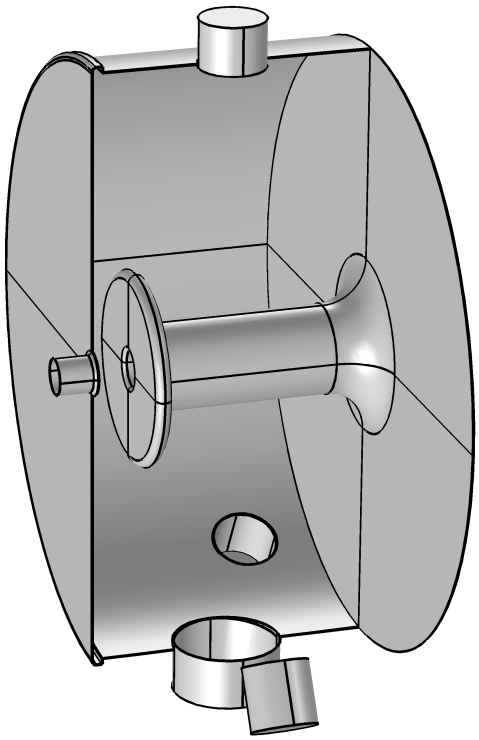

Figure 3.1: Internal shape of the 100 MHz cavities for MAX IV, extended with ports for power and HOM couplers.

the resonance frequencies of the cavity modes were not affected by the impedance boundary condition, see Table 3.1. The downside of using this boundary condition is that it is very time consuming, which is already a problem for the 3D solver. The upside of this boundary conditions is that it is easy for Comsol to calculate the Q-value and other useful entities, like the shunt resistance, and that they are also more accurate. Because of the very minor corrections to the frequencies and the hardware limitations, it was decided that PEC boundary conditions were good enough for finding the resonance frequencies.

3.2 Measurement setup

To measure the modes, a spectrum analyzer (Rohde & Schwarz FSL Spectrum Analyzer 9 kHz - 3 GHz) was used. This device was used in a way where it was connected to the two probe loops in the cavity to perform a transmission (S21) measurement. To accomplish this, the frequency analyzer generates an output signal which is swept over the desired frequency interval and sent to the first probe loop, whereafter the modes excited in the cavity by the resulting fields are coupled through the second probe loop and read back by the instrument. The instrument then plots a graph where the amplitude of the recieved signal is

Table 3.1: Comparison of the frequencies of a few example modes in the 100 MHz cavity using different boundary conditions in Comsol.

PEC	**IBC**
99.969	99.966
461.321	461.309
626.397	626.336
856.843	856.853
937.522	937.526
1004.302	1004.311
1195.000	1195.006
1243.282	1243.286
1301.506	1301.508

plotted as amplitude as a function of frequency, see Figure 3.2. The amplitude is here displayed in dBm relative to the input signal (0 dBm), which means that the values in the graph are negative, since the signal is attenuated. The whole measurement setup can be seen in Figure 3.3. It can be noted that the cavity model in Figure 3.1 is rotated 90 degrees around the symmetry axis with respect to the actual positioning, Figure 3.3, and viewed from the other side, to allow a better view of the internal structure.

3.2.1 Performing the measurements

To obtain the relevant information, peak frequency, f_r, and peak width, Δf, see Eq. (2.13), the amplitude span was, in general, set to 50 dBm and the frequency span to 1-2 MHz, whereafter the central frequency of the display was increased until a peak was seen. The values in Table A.1 gave some clue to where the resonances might be located, but the search was in fact conducted in the more thorough way described above. Once a peak had been found, it was zoomed in on to improve the resolution. The amplitude span was set to 5 dBm and the frequency span was set so that between -3 and -3.5 dBm from the top was visible. The peak frequency and the frequency values at -3 dBm from the peak value were then noted.

To get better values, most of the readings were done with the averaging function of the spectrum analyzer on, to reduce the noise. This function was set to average over the last 50 readings. Especially for very weak peaks, this made a lot of difference, whereas strong peaks were largely unaffected. The averaging was turned off when using the RF trombone, described below, because a more real-time view was then needed.

The spectrum was scanned in the interval from the fundamental frequency ($\approx$100 MHz) up to just above 1300 MHz. This was done at 3 different fundamental frequencies with 200-400 kHz spacing in between each, to examine how the HOMs "moved" relative to the fundamental mode. The change of frequency, or tuning,

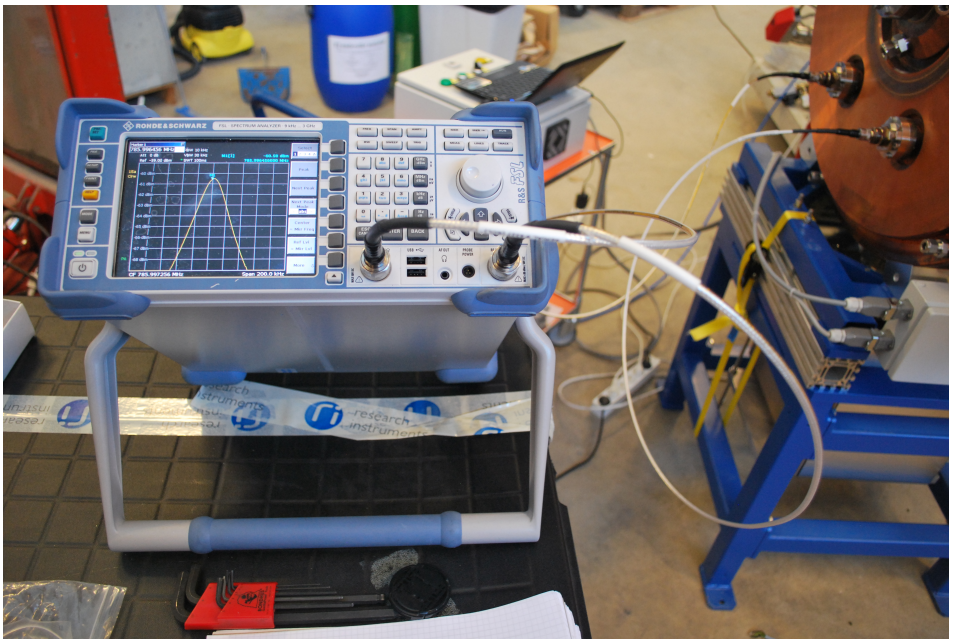

Figure 3.2: The spectrum analyzer. On the screen is a zoomed in resonance peak. To the upper right, the connections to the cavity can be seen.

of the cavity is done, both on the 100 MHz and harmonic cavities, by pushing one or both walls, for 100 MHz and harmonic, respectively, inwards or outwards by means of an electric motor. See Figure 3.4 for a picture of the tuning mechanism on the 100 MHz cavities. The internal displacement the tuning mechanism gives rise to is for these cavities up to ± 1 mm.

The first actual measurements were done on a cavity with an open (in the RF sense) transmission line, cf. Fig 3.3, but without the trombone and its adapter. We noticed that when we moved another cavity which was standing close to the open line, many of the peak values and widths changed by a rather large amount. This made the first round of measurements forfeit, except that we now knew that the resonances were greatly affected by what was connected to the cavity.

The next step we did was to attach the previously mentioned RF trombone to the transmission line to investigate how the resonances and their widths were affected by a change in length of the transmission line. The trombone is a device that allows a continuous change in length of such a transmission line by simply pulling one end out, see Figure 3.5. This enabled us to find the "worst case scenario", i.e. where the HOM peaks were as narrow as possible.

Our measurements showed that the length of the transmisson line had an even greater impact on some modes than was seen before. One trombone length, essentially one length of the transmission line, could produce a rather sharp resonance, while another length showed complete attenuation of the same resonance, see Figure 3.6. Of course, this change in length is wavelength dependent and so is

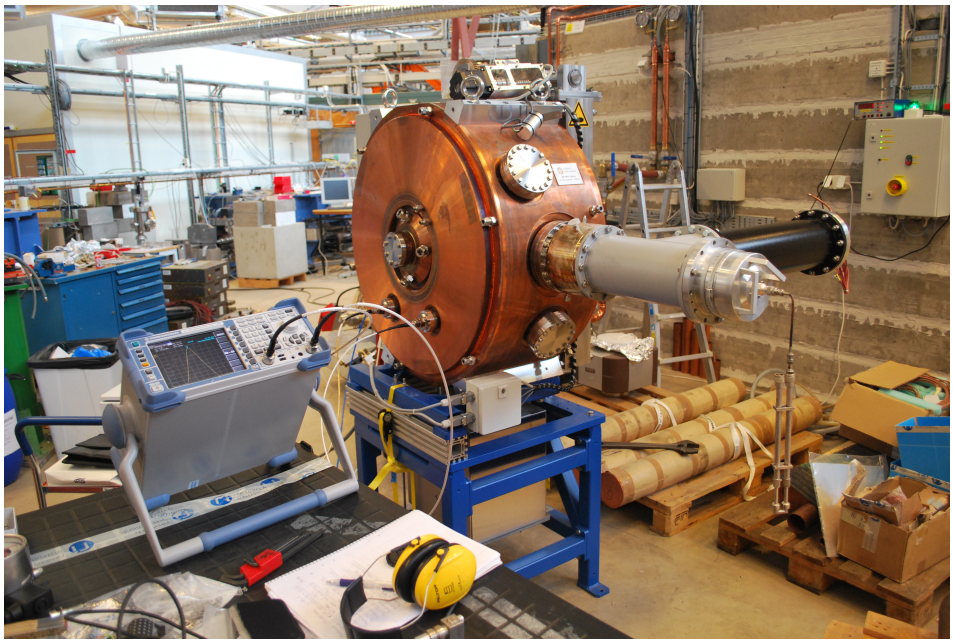

Figure 3.3: The measurement setup. To the front left is the spectrum analyzer and in the center is the cavity with the measurement cables connected. Going into the right side of the cavity is part of the transmission line through which the power is fed. At the end of the transmission line, an RF trombone is attached.

different for all modes. Also, some modes, most likely TE modes or other modes that do not couple well to the power coupling loop, were completely unaffected by the trombone.

After these measurements were done, the coupling loop was taken out of the cavity, see Figure 3.7. This was done to put it into another cavity which had previously had a leak at the ceramic window separating the vacuum in the cavity from the air in the transmission line. This gave us a good opportunity to measure the resonances for a cavity with just a blind flange attached instead of the transmission line. This is essentially what is described for the model in Section 3.1. This would provide a good test of the model. The measurement data for the cavity without transmission line can be seen in Table A.2 in Appendix A Subsection A.1.2.

Because the transmission line played such a significant role in the performance of the cavity, we decided that no further measurements were to be done on the 100 MHz cavities until we could measure on one that was connected to the actual RF system at the MAX IV site. Besides the transmission line, the RF system also contains a circulator and a transmitter from the power source. It is unknown how this setup behaves for HOMs.

Because of time restriction, a thorough measurement and analysis of the harmonic cavities was never done. This is an example of future work that can be done, see Chapter 6.

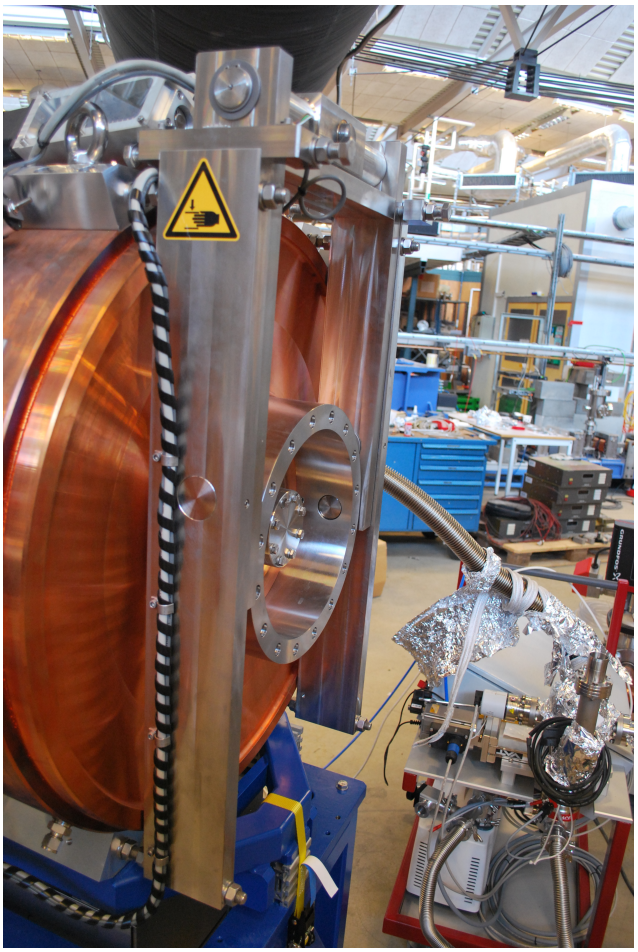

Figure 3.4: Tuning mechanism of the 100 MHz cavities. Moving the walls in or out changes the internal geometry and thus the resonance frequencies.

3.3 ZAP calculations

To calculate the mode growth in the cavities, the software ZAP [18] was used. This software calculates the spectrum of the beam and compares it to the cavity modes, which are input as separate data. ZAP uses this information to calculate the growth time of different rigid, longitudinal coupled bunch instability modes[1]. The code is fairly old and can only handle up to 20 different HOMs and only Gaussian or parabolic bunch shapes. Luckily, as seen in Table A.1, many shunt resistances were very small, so we could easily pick out the modes most likely to influence the beam. Of the two bunch shape choices, Gaussian is the one that fits

[1]The code can actually handle many more things, such as transverse instabilities, etc., but we had previously decided to focus on the longitudinal ones.

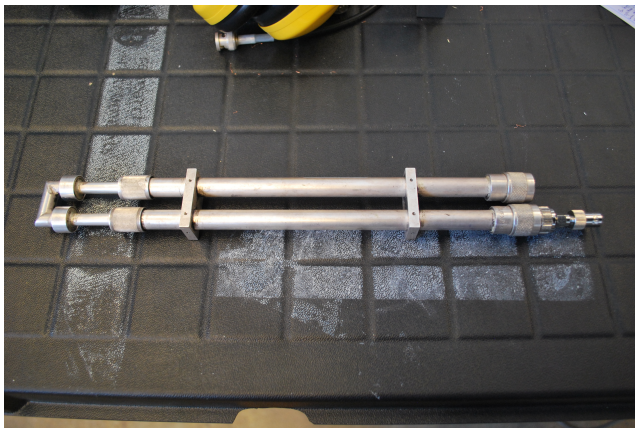

Figure 3.5: The RF trombone used for the measurements. The length is 25-30 cm with the extendable part extending up to ca 10 cm, which means a total change in line length of ca 20 cm.

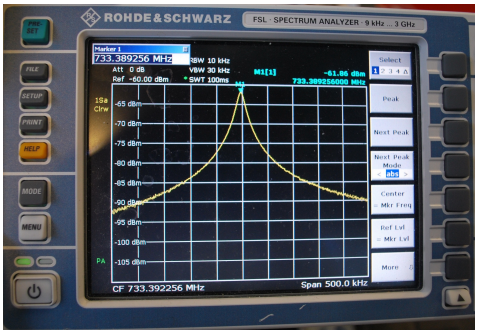

(a) Narrowest peak achievable for this mode.

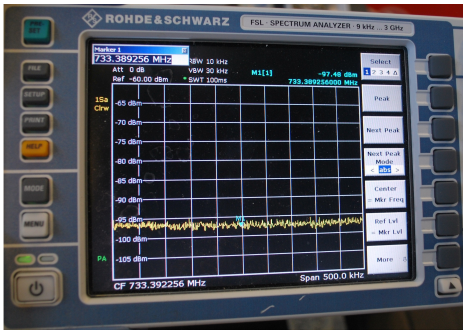

(b) Same peak at another trombone length.

Figure 3.6: The same peak at two different lengths of the trombone.

best, so this is the one we went with, even though it gives a different spectrum than the real shape.

ZAP calculates the complex coherent synchrotron frequency shift according to Eq. (2.20) and from that the growth rate, r_{gr}. There are two different outputs, one sorted after largest real frequency shift and one sorted after shortest growth time. Because the input data for the ZAP calculations needed to be analyzed and treated before the calculations could be run, the results of the ZAP runs are shown in Section 4.3.

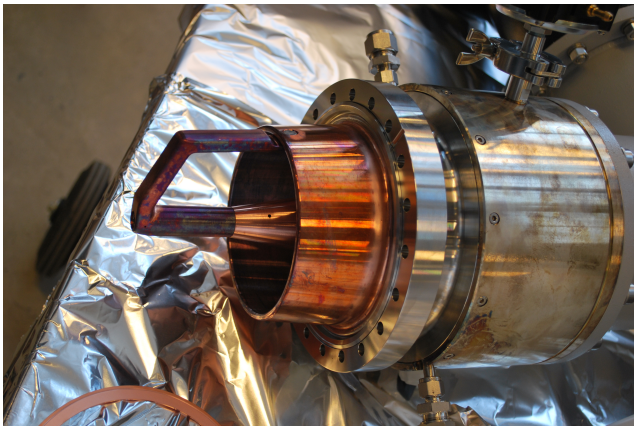

Figure 3.7: Coupling loop for the 100 MHz cavities. The inner conductor of the coax continues out into the loop and then goes back to attach to the outer conductor, a design made for coupling to the $\boldsymbol{B}$-field in the cavity.

Chapter 4
Analyzing the Data

In this chapter, we explain how we analyzed the theoretical and measured data.

4.1 Matching theory to measurements

We now have to match the data from both theoretical models and measurements to e.g. correct the shunt resistance to the correct mode. This is complicated for frequencies above 620 MHz, since the measured and theoretical results then start to deviate. This is likely due to missing elements in the model, such as the pump slots, which were predicted to have little to no effect on the lower modes. Luckily, there are some "solitary" modes in the spectrum, i.e. modes which have no very close neighbors, that one could try to match the spectrum from. Many of the previously axially symmetric modes are such solitary modes, and even more luckily, these are the ones with the largest shunt resistances.

Thus, we were able to match at least the first part of the spectrum as well as the modes with the largest shunt resistances and correct their values with the measured Q-values. To match more modes, and with higher certainty, one would have to extend the model further with the missing elements.

4.2 Tuning linearity

One important aspect when tuning the cavity is to know how the HOMs drift relative to the fundamental frequency. Using the frequency data from Table A.2, we set the HOM frequencies as a function of the fundamental frequency at the 3 tuning points. We then calculated a linear fit of the HOM values on the form

$$f_{HOM} = k_{fit}x + m_{fit},$$

which we then subtracted from the measured values at each tuning point, $x = f_{fundamental}$, to form the relative spectral offset. The relative spectral offset then tells us about how far from a linear movement of the HOMs we are. The resulting values can be seen in Table A.3 and a histogram of the values can be seen in Figure 4.1. If such a value is small, it means that the linear fit matches the HOM frequency dependence well. The average of this distribution is approximately $34 \cdot 10^{-6}$ MHz and the standard deviation is 0.0168 MHz, which is much less than one per mille

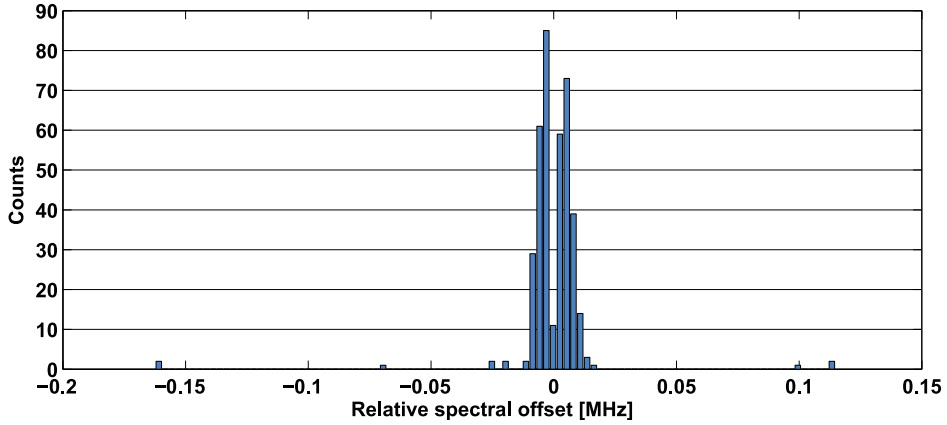

Figure 4.1: Histogram of the values in Table A.3.

of the absolute frequency. This means that even though we did not necessarily measure the cavity at exactly the nominal frequency 99.931 MHz, we can safely interpolate most of the data to find out which HOM frequencies we end up with for a given fundamental frequency. Only very few modes behave non-linearly.

It should be noted that the frequency data was measured at room temperature and without the coupling loop, but from an earlier, more incomplete measurement where the loop was present, we could also see the linear movement of the HOMs. The increased temperature during operation should only affect the absolute frequency of the individual peaks, not how they move during tuning. The temperature was assumed to be constant in the cavity. A non-constant temperature model needs more sophisticated measurements and calculations.

The values listed in Table A.2 were taken over several days, which means that there might be slow temperature fluctuations in the ambient temperature which would then look like HOM drift. This effect might also affect values measured during one single day. As can be seen in Table A.3, most of the values have small offsets with the general characteristic that the two end-points have the same sign and the center point has the opposite sign with respect to the end-points. We believe that this is a good example of this temperature dependence. The temperature has for some reason been different on the day that the center point was measured[1] and this has shifted the frequency with respect to the two other measurement days.

[1]During one of the measurement days, there was a lot of work going on inside the MAX II tunnel and the doors were left open. Since the temperature in the ring tunnel is kept at ca 28 °C, and the area enclosed by the ring is usually at room temperature, this will have caused the temperature to rise a bit. The values at the center point were, most of them, measured on 150330, which was a monday. On mondays the accelerator is usually down for maintenance, so we deem this scenario likely.

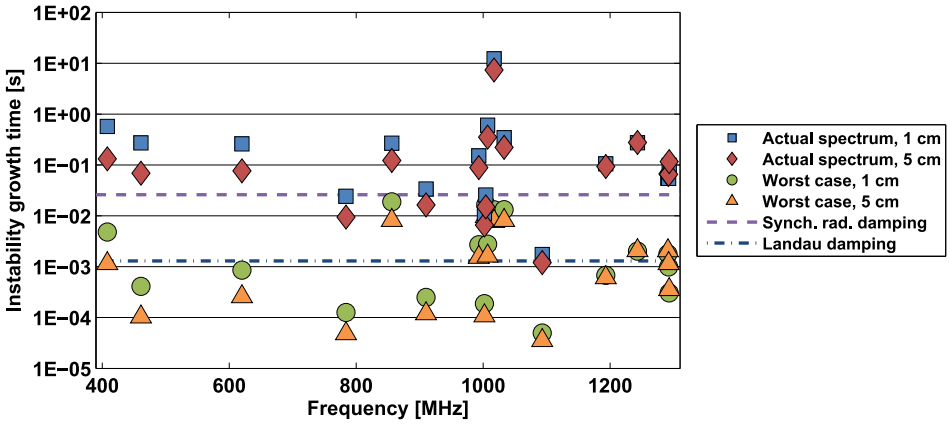

Figure 4.2: ZAP calculations for two different bunch lengths and two cases of cavity resonance frequencies for 100 MHz cavity 3170/6 without coupling loop.

4.3 Instabilities

This section describes the analysis and calculations that were done on the instabilities with the software ZAP. A short introduction to this software can be found in Section 3.3.

4.3.1 Initial calculations

The result of the ZAP calculations for the 100 MHz cavity 3170/6 can be seen in Figure 4.2. The data used was the f_2 and Q_2-values from Table A.2 and the shunt resistances from Table A.1, corrected with the Q_2-values from Table A.2. The calculations were run with two different bunch lengths of 1 and 5 cm, corresponding to without and with harmonic cavities, respectively. In one case, the actual spectrum of the Gaussian bunches was used and in the second, a "worst case" scenario was established by the code by moving the cavity resonances to the nearest beam spectrum peak. Figure 4.2 also shows the damping times for synchrotron radiation damping and Landau damping, to which the growth times need to be compared.

Some of the theoretical modes could not be matched to the measured ones for different reasons, see Section 4.1, so for those the theoretical frequencies and Q-values were used instead. This means that the frequencies might be off by as much as 2 MHz, and that the shunt resistances are overestimated. Table 4.1 lists the different HOM frequencies, f, the worst case frequencies, f_{wc}, as well as whether the worst case frequency is within the frequency range during mechanical tuning and wheter the worst case frequency growth times are below Landau damping.

Table 4.1: Frequencies of the HOMs used in ZAP as well as whether the worst case frequencies are within the respective frequency intervals during mechanical tuning and whether the worst case frequency growth times are below Landau damping. An asterisk, *, denotes modes that have theoretical frequencies and Q-values.

f [MHz]	f_{wc} [MHz]	f_{wc} in span	τ_{gr} below damping
408.744	408.808	No	Yes
461.213	461.044	No	Yes
620.447	620.593	No	Yes
784.263	784.116	Yes	Yes
856.267	856.225	Yes	No
910.897	910.733	Yes	Yes
993.127	993.063	No	No
1002.804	1002.715	Yes	Yes
1004.498	1004.418	Yes	No
1007.561	1007.825	No	No
1017.086	1016.910	No	No
1033.421	1033.376	Yes	No
1093.470*	1093.561	N/A	Yes
1193.301	1193.492	No	Yes
1243.847	1244.025	No	No
1291.200*	1291.152	N/A	No
1292.360*	1292.287	N/A	Yes
1293.600*	1293.423	N/A	Yes

4.3.2 Including the temperature dependence

The values used for the previous calculations were measured at ca 22 °C, but the working temperature of the active cavities will be within the temperature span 30-60 °C. Because we were not able to do any measurements at the MAX IV site, to get a better estimate of the growth rates, we need to correct the frequencies, Q-values and shunt resistances to better match the real case. While we do not simulate the effect of the coupling loop, this should mostly affect the Q-values. Q-values and shunt resistances change with temperature mostly because of the change in surface resistance, while the small change in volume due to thermal expansion should be the largest reason for changes in frequency.

The following linear model for the change in frequency was used [15]:

$$f(T) = f_0 \left(1 - \alpha(T - T_0)\right),$$

where f_0 is the frequency at 22 °C, $\alpha = 1.66 \cdot 10^{-5}$ is the thermal expansion coefficient for copper, T is the actual temperature and T_0 is the temperature where f_0 was measured. In this way, we modeled the change of temperature to 45 °C, which lowered all frequencies, and then "tuned" the fundamental mode back to its nominal frequency, 99.931 MHz. Because we had information about how the HOMs move during tuning, see Section 4.2, we obtained estimates for the frequencies of all HOMs at higher temperature. This scheme follows the same principles as a real temperature tuning scheme and allows us to keep the fundamental frequency the same while changing the frequencies of the HOMs.

For the Q-values and shunt resistances, the temperature dependence stems from the change in material resistivity, which affects the surface resistance, see Eqs. (2.14), (2.15) and (2.17). Since $R_S = \sqrt{\frac{\omega\mu_0}{2\sigma_c}}$ and $\sigma_c = 1/\rho_c$, with ρ_c being the resistivity, we can directly use the following linear model for the resistivity [12]

$$\rho(T) = \rho_0 \left(1 + \xi(T - T_0)\right),$$

where $\rho_0 = 1.68 \cdot 10^8$ is the resistivity measured at the reference temperature T_0 (usually 20 °C) and $\xi = 0.003862$ is an empirical parameter fitted from measurement data. For 45 °C, we get that the surface resistance changes by a factor of $\sqrt{(1 + \xi(T - T_0))} \approx 1.0472$, which makes the Q-values and shunt resistances change by the same factor.

After correcting the input values, the same ZAP calculations were run again and new results were obtained, see Figure 4.3. In Table 4.2, we list the actual cavity spectrum frequencies after temperature correction, f, and worst case frequencies, f_{wc}. We also checked whether the worst case frequency is within the frequency range, the range of frequencies the HOM can take during temperature tuning (30-60 °C), and wheter the worst case frequency growth times are below Landau damping. If the worst case frequency lies within the frequency range, it means that it is possible to cross it at some point during temperature tuning, which could then cause the HOM to start driving a previously damped instability. If this instability also has a growth time which is below Landau damping, we have a potentially dangerous situation. One interesting point that can be made here is that although the HOM frequencies change when we change temperature and tune the cavity, not all the worst case frequencies change, cf. Table 4.1.

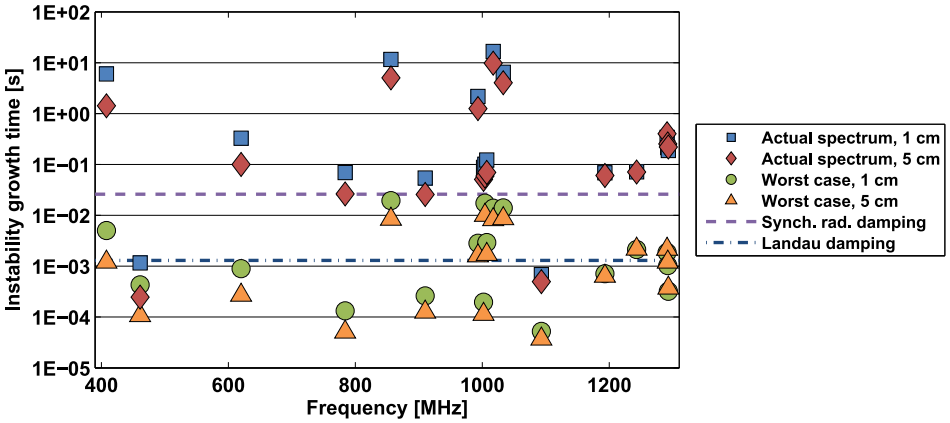

Figure 4.3: ZAP calculations for two different bunch lengths and two cases of cavity resonance frequencies for 100 MHz cavity 3170/6 without coupling loop. The values used for this round of calculations were corrected to the operating temperature of 45 $^{\circ}C$.

One major similarity between Figures 4.2 and 4.3 is that we in both pictures have the HOM at 1093 MHz around or below Landau damping, even with the actual spectrum, which means that this instability is not Landau damped. While one should keep an eye on this in future measurements, it is not necessary to take this mode very seriously at the moment, as it is one of the theoretical ones, i.e. frequency, Q-value and shunt resistance are completely theoretical. In the future, a better matching between theory and measurement might show that this mode is off by several 100 kHz, even some MHz, and the Q-value and shunt resistances will be lower.

One major difference between the Figures is that the instability at 461 MHz has gone down severely in growth time. This is a good example of how things can change when the conditions in the cavity change; the general behaviour of instabilities with the actual spectrum is that growth times go up, partly because Q-values and shunt resistances go down, but this one mode takes a dive of more than 2 orders of magnitude and is suddenly not Landau damped anymore. One possible solutions to this problem is to change the temperature further in either direction, while still keeping the fundamental frequency constant, and examine how this mode behaves then.

Table 4.2: Frequencies of the HOMs (after temperature correction) used in ZAP as well as whether the worst case frequencies are within the respective frequency intervals when temperature tuning (30-60 °C) and whether the worst case frequency growth times are below Landau damping. An asterisk, *, denotes modes that have theoretical frequencies and Q-values.

f [MHz]	f_{wc} [MHz]	f_{wc} in span	τ_{gr} below damping
408.592	408.808	No	Yes
461.037	461.044	Yes	Yes
620.197	620.025	No	Yes
783.866	784.116	Yes	Yes
855.940	855.658	No	No
910.524	910.733	No	Yes
992.743	992.495	Yes	No
1002.401	1002.147	No	Yes
1004.089	1003.851	Yes	No
1007.138	1007.257	Yes	No
1016.703	1016.910	Yes	No
1033.008	1032.808	Yes	No
1093.052*	1092.993	N/A	Yes
1192.767	1192.924	Yes	Yes
1243.366	1243.457	Yes	No
1290.707*	1290.584	N/A	No
1291.867*	1291.719	N/A	Yes
1293.106*	1292.855	N/A	Yes

Chapter 5

Summary and conclusions

We measured the full HOM spectrum of a MAX IV 100 MHz cavity up to ca 1300 MHz and the measured peaks were compared to the theoretical frequencies. While not all peaks could be identified, the most important ones, i.e. the ones with a possibly large impact on the beam, could be identified and studied. By correcting the theoretical shunt resistances and Q-values with the measured Q-values, we obtained values for the "real" shunt resistances. The assumption used to do this was that the fraction R_{sh}/Q is fairly independent of deficiencies in the surface structure of the cavity and mostly dependent on the actual mode and the general geometry.

We tried to predict the shift of the whole HOM spectrum when changing the cavity temperature from the measurement temperature of roughly 22 °C to its operating temperature of 45 °C. This was done by using the fact that we know the temperature dependence of the mode frequencies for small changes of temperature, and by using our measured linear dependence on the mode frequency shifts during mechanical tuning of the cavity.

A beam instability study was also performed with the code ZAP, both for the HOMs at the frequencies measured at room temperature and for the predicted frequencies at operating temperature. By doing this, one can estimate how much the instabilities are affected by temperature tuning of the cavity. The instability study had to be limited to rigid longitudinal coupled bunch instabilities to fit withing the time limit and scope of the thesis work. The data and methods presented in this thesis allow for further studies of rigid transverse coupled bunch instabilities and also for coupled bunch instabilities of higher order, where the bunch shapes could oscillate at multiples of the synchrotron frequency.

Chapter 6
Future work

This chapter descibes the future work that can, and to some extent will, be done to make a more complete analysis of this part of the MAX IV 3 GeV ring.

- The level of detail in the Comsol model should be increased, i.e. the pump slots and maybe even the ports for the coupling loops should be included. As discussed earlier, this requires more RAM than what is available at the moment. One option here is to use the Lund University computing cluster, Lunarc [22]. Another is to get an upgraded computer, but this is most likely harder to motivate.
- Full measurements of the spectra should be done at the MAX IV site, with connected transmission lines and for all available cavities. The spectra should be measured at three different temperature points to enable linearity study. This data should then be used in an extended instability study (see below).
- Full measurements and analyses of the harmonic cavities should be done in the same way as for the active cavities. However no considerations regarding a transmission line and coupling loop are needed.
- The effect of the $\boldsymbol{B}$-field should be taken into account and studies on transverse instabilities conducted.
- Higher order synchrotron oscillations ($a > 1$) should be included in the calculations.
- The spectrum of the actual simulated bunch shape could be calculated and more realistic calculations, with the flat potential from the harmonic cavities, could be made. This need other methods than those used here.
- Studies could be conducted for the 1.5 GeV ring also. The cavities are the same, but because they also have individual discrepancies from the theoretical shape, a measurement series is necessary. Furthermore, the instability study needs to take into account the beam properties of this ring.

Acknowledgements

Finally, I would like to acknowledge the following:

Åke Andersson, for supervising me during this thesis work and, besides helping me with the things that were directly related to the thesis, showing me more practically oriented things around accelerator technology.

Anders Karlsson and David Olsson, for helping me with frustrating Comsol problems. Anders also provided much needed discussions around electromagnetic theory, and helped me a lot with the bureaucracy around getting my degree.

Magnus Sjöström and Francesca Curbis, for answering some of my many and diverse questions, and for sharing their office with me.

Martin Johansson, for supervising me during my work on the IPAC'15 article and presentation, which, although unrelated to the thesis, helped me improve my academic writing and gave me important experience.

Robert Lindvall and Lars Malmgren, for discussions around RF systems.

Anders J Johansson and the EIT radio lab, for lending me their trombone.

Jonas Breunlin, Galina Skripka, Teresia Olsson, Alan Mak, Olivia Karlberg, Walan Grizolli, Christian Stråhlman and Joel Andersson, for joining me for lunch and coffee breaks almost every day, for game nights, and for providing some distraction from the harsh real world. Special thanks to Jonas and Galina for discussions around the thesis work and for helping me find reading material and Joel for discussions around Comsol-related issues.

Pedro Fernandes Tavares and Simon Leemann, for answering many questions and helping me with writing and referencing.

Roger Nilsson, for suggesting that I should apply for summer work at MAX IV Laboratory in the summer of 2013, and before that employing me himself, which has benefitted me in so many ways.

Everyone in LEG (you know who you are), for putting up with me for the better part of my 5 years at LTH.

Last but not least, my family, for being there for me.

References

[1] *Max IV Highlights and activities 2013*, MAX-lab, https://www.maxlab.lu.se/sites/default/files/MAX%20IV_H&A_2013_0.pdf, (Retrieved 2015-06-12

[2] K. Wille, *The Physics of Particle Accelerators, An Introduction*, Oxford, United Kingdom, Oxford University Press, ISBN 0-19-850549-3, 2005

[3] E. Wallén, "MAX IV Detailed Design Report", ch. 5, https://www.maxlab.lu.se/sites/default/files/Insertion_Devices_MAXIV_3GeV_Ring_Feb_2010.pdf

[4] M. Eriksson et al., "Challenge of MAX IV towards a multi purpose highly brilliant light source", in the *Proceedings of 2011 Particle Accelerator Conference*, pp. 737-741, New York, NY, USA

[5] P. F. Tavares et al., "The MAX IV storage ring project", *Journal of Synchrotron Radiation*, vol. 21, no. 5, pp. 862-877, ISSN 1600-5775, September 2014

[6] E. Elafifi et al., "An electron gun test stand to prepare for the MAX IV project", in the *Proceedings of 2012 International Particle Accelerator Conference*, pp. 1551-1553, New Orleans, LA, USA

[7] *Max II*, MAX-lab, https://www.maxlab.lu.se/node/277, (Retrieved 2015-06-12)

[8] M. Johansson et al., "Magnet design for a low-emittance storage ring", *Journal of Synchrotron Radiation*, vol. 21, no. 5, pp. 884-903, ISSN 1600-5775, September 2014

[9] J. Björklund Svensson, M. Johansson, "Relative alignment within the MAX IV 3 GeV storage ring magnet blocks", in the *Proceedings of 2015 International Particle Accelerator Conference*, currently in pre-press, Richmond, VA, USA

[10] S. Y. Lee *Accelerator Physics* Toh Tuck, Singapore, World Scientific Publishing, ISBN 978-981-4374-94-1, 2012

[11] A. Karlsson, G. Kristensson, *Microwave Theory*, Lund, Sweden, KFS i Lund AB, Compendium, 2014

[12] *Electrical resistivity and conductivity*, Wikipedia, http://en.wikipedia.org/wiki/Electrical_resistivity_and_conductivity, (Retrieved 2015-06-10)

[13] *Magnetic materials*, Microwaves101, http://www.microwaves101.com/encyclopedias/magnetic-materials, (Retrieved 2015-06-10)

[14] COMSOL AB, Stockholm, Sweden

[15] T. Moreno, *Microwave Transmission Design Data*, Norwood, MA, USA, Artech House, ISBN 978-0-89006-346-0, 1988

[16] H. Wiedemann, *Particle Accelerator Physics*, ch. 1, Berlin Heidelberg, Germany, Springer-Verlag, ISBN 978-3-540-49043-2, 2007

[17] S. Khan, *Collective Phenomena in Synchrotron Radiation Sources*, Berlin Heidelberg, Germany, Springer-Verlag, ISBN 978-3-540-34312-7, 2006

[18] M. S. Zisman et al., *ZAP User's Manual*, Berkeley, CA, USA, University of California Berkeley, 1986

[19] "MAX IV Detailed Design Report", ch. 2.2, https://www.maxlab.lu.se/sites/default/files/maxiv_ddr_2_2_Linear_Lattice_101122.pdf

[20] A. Hofmann, S. Meyers, "Beam Dynamics in a Double RF System", in the *Proceedings of 1980 International Conference on High-energy Accelerators*, pp. 610-614, Geneva, Switzerland

[21] S. Krinsky, J. M. Wang, "Longitudinal Instabilities of Bunched Beams Subject to a non-Harmonic RF Potential", *Particle Accelerators*, vol. 17, pp. 109-139, 1985

[22] *Center for scientific and technical computing at Lund University, Lunarc*, Lunarc, http://www.lunarc.lu.se/, (Retrieved 2015-06-11)

Appendix A

Appendix

A.1 All theoretical and measurement data

A.1.1 Data from extended 3D model

Table A.1: Data from the evaluations of the extended 3D model. We here see the obtained resonance frequencies of the evaluations, Q-values according to Eq. (2.12), shunt resistances according to Eq. (2.15) and (2.16) and corrected shunt resistances according to Eq. (2.18). Modes corresponding to axially symmetric ones are marked with an asterisk, *. The # column is for crossreferencing the modes with Table A.2. Not all modes could be matched, hence the missing numbers.

#	**Mode type**	f_r [MHz]	Q_{PEC}	R_{sh} [kOhm]	R_{corr} [kOhm]
1	TM*	99.8966	20965	3532	3368
2	TM*	408.167	33981	25	N/A
3	TM	419.151	29230	0	0
4	TM	419.769	29134	0	0
5	TM*	461.185	36076	262	257
6	TM	469.181	42737	1	1
7	TM	470.335	42688	0	N/A
8	TM	529.689	54811	0	0
9	TM	531.978	55550	0	0
10	TM	553.845	28001	0	0
11	TM	554.660	28073	0	0
12	TM	600.128	62304	0	0
13	TM	601.267	62392	0	N/A
14	TM*	620.835	30097	76	92
15	TE*	624.571	70294	0	-
16	TM	627.664	61531	0	-
17	TM	630.560	60157	0	-
18	TM	656.818	44126	0	-

Continued on next page

Table A.1 – continued from previous page

#	**Mode type**	f_r [MHz]	Q_{PEC}	R_{sh} [kOhm]	R_{corr} [kOhm]
19	TM	657.548	43818	0	-
21	TM	717.221	42206	0	-
22	TM	717.803	42298	0	-
23	TM	729.597	59297	0	-
24	TM	733.015	59938	0	-
25	TM	734.328	60164	0	-
26	TM	736.566	62052	0	-
27	TM	740.902	75829	0	-
28	TM	742.116	75879	0	-
29	TM*	784.310	39267	527	501
30	TM	818.672	48540	0	-
31	TM	819.625	47983	0	-
32	TM	837.174	59430	0	-
33	TM	842.013	52521	0	-
34	TM	842.395	52769	0	-
35	TM	846.401	49888	3	-
36	TM	848.389	62946	0	-
37	TM	851.667	51544	0	-
38	TM*	854.822	48460	4	-
40	TM	869.777	80159	0	-
41	TM	870.420	78267	3	-
42	TM	880.206	83922	4	-
43	TM	881.647	61643	0	-
44	TM	882.055	50129	0	-
45	TM	882.247	63088	0	-
47	TM*	910.306	41034	278	220
49	TM	928.786	59160	2	-
50	TM	931.315	61853	0	-
51	TE*	936.905	83518	0	-
52	TM	939.207	44024	1	-
53	TM	940.690	44663	0	-
54	TM	947.979	58515	0	-
55	TM	954.880	53967	0	-
56	TM	957.435	55097	0	-
57	TM	962.467	63698	0	-
58	TM	967.412	57703	0	-
59	TM	968.219	58003	0	-
60	TM	978.155	55842	0	-
61	TM	978.388	55573	0	-
62	TE*	988.755	84918	0	N/A
63	TM	992.219	65258	21	19
64	TM	994.627	65874	1	1

Continued on next page

Table A.1 – continued from previous page

#	**Mode type**	f_r [MHz]	Q_{PEC}	R_{sh} [kOhm]	R_{corr} [kOhm]
65	TM	1001.02	108634	3	1
66	TM*	1001.95	43753	268	N/A
67	-	1004.70	73519	47	3
68	-	1005.59	75729	71	-
69	-	1007.52	59782	39	18
70	-	1016.65	88855	4	N/A
71	-	1019.68	90832	0	0
72	-	1033.89	58504	4	-
73	-	1035.65	60495	0	-
74	-	1038.66	81812	0	-
75	-	1043.43	81020	0	-
76	-	1063.04	60039	0	-
77	-	1069.62	56013	1	-
78	-	1073.51	54552	0	-
79	-	1076.91	62967	0	-
80	-	1077.40	55911	0	-
81	-	1079.49	56476	0	-
82	-	1080.49	57434	0	-
83	-	1080.99	57296	0	-
84	-	1087.91	59917	0	-
85	-	1089.47	60283	0	-
86	TM*	1093.47	34409	932	-
87	-	1094.57	62528	2	-
88	-	1094.84	62321	0	-
89	-	1135.53	84561	2	-
90	-	1138.72	86296	0	-
91	-	1139.29	114490	0	-
92	-	1147.89	133000	0	-
93	-	1149.99	92925	2	-
94	-	1155.16	96417	0	-
95	-	1163.19	75647	2	-
96	-	1163.68	79320	0	-
97	-	1176.25	59668	4	-
98	-	1177.01	60798	1	-
99	-	1179.42	61392	0	-
100	-	1180.47	59318	0	-
101	-	1181.13	60190	0	-
102	-	1184.38	62581	4	-
103	-	1186.39	62837	3	-
104	-	1189.75	61316	4	-
105	TM*	1192.16	44175	73	63
106	-	1200.18	54507	1	-

Continued on next page

Table A.1 – continued from previous page

#	**Mode type**	f_r [MHz]	Q_{PEC}	R_{sh} [kOhm]	R_{corr} [kOhm]
107	-	1202.90	55318	0	-
108	-	1209.95	66967	0	-
109	-	1210.43	68210	0	-
110	-	1210.89	89337	0	-
111	-	1214.77	102048	0	-
112	-	1220.99	65101	0	-
113	-	1221.47	65249	0	-
114	TE*	1226.28	95416	0	-
115	-	1239.71	49658	2	-
116	-	1240.19	49408	0	-
117	TM*	1241.14	52969	27	20
119	-	1254.30	64393	4	-
120	-	1256.10	64249	0	-
121	-	1259.73	54488	1	-
122	-	1260.21	52625	0	-
123	-	1267.21	61896	3	-
124	-	1268.84	88870	0	-
126	-	1272.89	61403	2	-
127	-	1278.87	69529	6	-
128	-	1280.35	70805	1	-
129	-	1281.43	73932	4	-
130	-	1282.28	70100	0	-
131	-	1282.75	71085	2	-
132	-	1286.39	91718	13	-
133	-	1286.48	132232	1	-
134	-	1287.11	95713	2	-
135	-	1288.50	100734	0	-
136	-	1291.20	74972	23	-
137	-	1292.36	66764	41	-
138	TM*	1293.60	65723	131	-
139	-	1296.25	82761	7	-
140	TE*	1301.38	80263	1	-
141	-	1302.43	59850	15	-
142	-	1303.27	58943	7	-

A.1.2 Data from measurements on 100 MHz cavity 3170/6 without coupling loop

Table A.2: Data from measurements on 100 MHz cavity 3170/6 without coupling loop. The indexed numbers refer to the different tuning points of the fundamental frequency. The **[**# column is for cross referencing the (center) modes with Table A.1. Not all modes could be matched, hence the missing numbers.

#	f_1	Q_1	f_2	Q_2	f_3	Q_3
1	99.682	20343	99.9421	19988	100.3611	20072
2	-	-	408.744	-	408.788	-
3	419.338	27956	418.799	27920	417.944	27863
4	419.787	27986	419.249	27950	418.399	27893
5	461.241	35480	461.213	35478	461.182	35476
6	469.620	27625	469.702	29356	469.852	29366
7	470.740	-	470.816	-	470.952	-
8	527.191	43933	526.968	43914	526.626	43886
9	530.445	48222	530.217	48202	529.867	48170
10	554.040	26383	553.895	26376	553.673	27684
11	554.544	24111	554.412	25201	554.220	25192
12	600.480	60048	600.520	60052	600.599	60060
13	601.715	26162	601.775	-	601.835	-
14	620.559	36503	620.447	36497	620.276	38767
15	621.463	51789	621.303	56482	621.060	56460
16	621.808	29610	621.880	23918	622.014	-
17	627.490	52291	627.352	52279	627.149	52262
18	656.488	34552	656.440	34549	656.384	34547
19	657.199	38659	657.155	41072	657.104	41069
20	715.234	9054	715.146	9933	715.023	9662
21	718.364	39909	718.201	39900	717.952	39886
22	718.904	12612	718.744	21140	718.501	29938
23	725.954	-	725.875	-	725.770	-
24	733.350	48890	733.260	48884	733.134	48876
25	733.552	38608	733.463	40748	733.340	43138
27	741.505	61792	741.531	61794	741.586	61799
28	742.469	67497	742.498	74250	742.556	74256
29	785.007	37381	784.263	37346	783.100	37290
31	822.081	5872	821.826	5479	821.451	5009
32	836.966	3182	836.896	3021	836.812	3088
33	837.816	5859	837.739	5660	837.644	5584
34	843.173	49598	843.088	49593	842.964	49586
35	843.879	46882	843.797	46878	843.687	46871
36	846.437	44549	846.044	44529	845.437	44497

Continued on next page

Table A.2 – continued from previous page

#	f_1	Q_1	f_2	Q_2	f_3	Q_3
37	851.527	50090	851.119	50066	850.496	50029
38	856.315	40777	856.267	38921	856.211	38919
39	863.859	14162	863.715	14892	863.508	15420
40	865.728	24048	865.537	24043	865.256	24035
41	875.791	13684	875.664	13268	875.484	13265
42	880.561	48920	880.558	48920	880.568	46346
43	882.422	21010	882.421	16970	882.431	13171
44	882.955	10388	882.908	11036	882.866	13583
45	883.639	42078	883.669	42079	883.737	42083
46	883.752	42083	883.782	44189	883.850	46518
47	911.133	31418	910.897	32532	910.548	33724
48	913.603	7251	913.564	7488	913.533	7250
49	927.711	9277	927.590	10422	927.346	14051
50	929.030	20645	928.747	18211	928.392	13263
51	931.807	20257	931.478	23884	930.961	28211
52	937.517	49343	937.087	46854	936.441	40715
53	938.210	15380	937.995	15898	937.638	17364
54	943.956	12586	943.779	11103	943.492	11100
55	956.086	50320	955.878	50309	955.532	50291
56	958.546	50450	958.340	50439	957.989	50420
57	966.740	-	966.667	-	966.588	-
58	968.834	37263	968.775	38751	968.656	40361
59	969.441	11016	969.385	11016	969.282	11015
60	978.737	51512	978.386	51494	977.808	48890
61	978.869	25760	978.523	26447	977.955	31547
62	987.327	-	987.243	-	987.115	-
63	993.118	58419	993.127	58419	993.121	58419
64	995.680	62230	995.692	62231	995.688	62230
65	1002.093	37115	1001.999	37111	1001.827	35780
66	1002.989	-	1002.804	-	1002.528	-
67	1004.726	4101	1004.498	4672	1004.155	5804
69	1007.801	28794	1007.561	27988	1007.164	27977
70	1017.112	-	1017.086	-	1017.073	-
71	1020.407	85034	1020.426	85035	1020.433	85036
72	1033.588	-	1033.421	-	1033.171	-
73	1035.518	-	1035.370	-	1035.168	-
74	1036.624	19197	1036.424	16451	1036.092	11022
75	1052.704	-	1052.636	-	1052.551	-
76	1062.351	-	1062.290	-	1062.175	-
77	1070.107	24321	1070.007	23778	1069.816	24879
78	1071.352	26131	1071.275	26782	1071.123	28187
79	1076.756	9970	1076.646	11703	1076.440	15601

Continued on next page

Table A.2 – continued from previous page

#	f_1	Q_1	f_2	Q_2	f_3	Q_3
80	1079.389	4200	1079.126	4199	1078.684	4532
81	1080.669	13179	1080.352	10489	1079.850	7296
82	1081.516	27038	1081.322	27726	1080.990	28447
83	1082.503	-	1082.293	2195	1082.602	-
84	1087.917	10771	1087.749	11099	1087.444	11569
85	1089.798	54490	1089.655	54483	1089.376	54469
-	1095.170	-	-	-	-	-
87	1095.537	47632	1095.436	47628	1095.280	47621
88	1095.987	47652	1095.914	47648	1095.790	52180
89	1136.281	75752	1136.287	75752	1136.268	75751
91	1139.266	54251	1139.274	54251	1139.262	56963
-	1149.600	-	-	-	-	-
92	1150.189	71887	1150.149	71884	1150.057	71879
93	1153.875	10395	1153.779	10302	1153.598	10883
94	1155.953	96329	1155.963	88920	1155.949	88919
95	1164.066	48503	1163.973	48499	1163.800	48492
96	1165.833	6406	1165.725	6549	1165.528	6548
97	1174.960	41963	1174.816	41958	1174.556	41948
98	1177.357	53516	1177.225	53510	1176.983	53499
99	1180.403	34718	1179.978	33714	1179.277	32758
100	1181.110	42182	1180.639	43727	1179.859	47194
102	1185.091	42325	1184.819	45570	1184.355	49348
103	1186.286	4477	1186.144	4688	1185.876	5490
104	1187.913	12912	1187.664	10797	1187.280	8188
105	1193.769	38509	1193.301	38494	1192.515	39751
106	1200.472	-	1199.700	-	1198.487	15565
107	1203.461	48138	1202.683	48107	1201.412	48056
109	1211.460	-	1211.298	-	1211.068	-
110	1211.785	60589	1211.653	60583	1211.416	60571
111	1219.759	8903	1219.691	8838	1219.544	8240
112	1222.606	30565	1222.550	30564	1222.435	29815
113	1222.936	55588	1222.878	58232	1222.761	58227
114	1226.408	12264	1226.228	13045	1225.911	13774
116	1242.564	27012	1242.284	27606	1241.813	32679
117	1243.851	42891	1243.847	40124	1243.823	36583
118	1244.206	7406	1244.202	9216	1244.172	9285
119	1254.596	14588	1254.002	17914	1253.000	21603
120	1256.463	-	1255.820	-	1254.799	-
121	1259.615	8871	1259.253	7870	1258.665	7404
123	1266.295	27528	1266.069	28135	1265.680	28765
124	1266.977	14397	1266.863	14396	1266.651	15261
125	1271.991	-	1271.915	-	1271.876	5628

Continued on next page

Table A.2 – continued from previous page

#	f_1	Q_1	f_2	Q_2	f_3	Q_3
126	1272.516	33487	1272.398	31034	1272.179	20193
127	1277.752	34534	1277.669	33623	1277.496	29709
128	1281.304	64065	1280.991	64050	1280.453	67392
129	1282.059	53419	1281.736	53406	1281.190	51248
130	1282.721	47508	1282.492	55761	1282.099	61052
131	1283.751	38902	1283.555	40111	1283.216	36663
132	1287.002	85800	1286.991	85799	1286.935	80433
133	1287.959	67787	1287.961	61331	1287.925	49536
134	1288.713	11716	1288.643	11932	1288.508	12510
135	1289.377	80586	1289.396	85960	1289.397	85960
136	1291.997	68000	1291.879	67994	1291.657	67982
138	1293.296	61586	1293.126	61577	1292.804	61562
-	1294.850	47957	-	-	1294.436	46230
139	1298.022	6691	1297.324	-	1295.742	3314
142	1304.730	50182	1304.660	48321	1304.520	48316
143	1305.887	54412	1305.808	54409	1305.655	52226

A.1.3 Data from HOM drift linearity check

Table A.3: Results of the linear fit subtraction (relative spectral offset) described in Section 4.2. The frequencies used are the frequencies in Table A.2. The blank spaces are due to one or more missing frequencies. The right-most column is the k-parameter in the linear fit, i.e. a measure of how sensitive the actual mode is to tuning. Non-linear modes are marked with ▲.

f_2 [MHz]	**Point 1** [MHz]	**Point 2** [MHz]	**Point 3** [MHz]	k
408.744	-	-	-	
418.799	0.0021	-0.0033	0.0013	
419.249	0.0026	-0.0042	0.0016	
461.213	0.0022	-0.0035	0.0014	
469.702	0.0028	-0.0045	0.0017	
470.816	0.0021	-0.0034	0.0013	
526.968	0.0027	-0.0043	0.0017	
530.217	0.0027	-0.0043	0.0017	
553.895	0.0018	-0.0029	0.0011	
554.412	0.0032	-0.0052	0.0020	
600.520	0.0023	-0.0037	0.0014	
601.775	-0.0057	0.0092	-0.0035	
620.447	0.0015	-0.0024	0.0009	
621.303	0.0023	-0.0037	0.0014	
621.880	0.0028	-0.0045	0.0017	
627.352	0.0030	-0.0048	0.0019	
656.440	0.0033	-0.0053	0.0020	
657.155	0.0031	-0.0050	0.0019	
715.146	0.0029	-0.0047	0.0018	
718.201	0.0021	-0.0034	0.0013	
718.744	0.0023	-0.0037	0.0014	
725.875	0.0034	-0.0056	0.0021	
733.260	0.0029	-0.0048	0.0018	
733.463	0.0032	-0.0051	0.0020	
741.531	0.0020	-0.0033	0.0013	
742.498	0.0017	-0.0028	0.0011	
784.263	0.0055	-0.0089	0.0034	
821.826	0.0055	-0.0090	0.0034	
836.896	0.0045	-0.0072	0.0028	
837.739	0.0045	-0.0073	0.0028	
843.088	0.0020	-0.0032	0.0012	
843.797	0.0034	-0.0055	0.0021	
846.044	0.0040	-0.0065	0.0025	
851.119	0.0053	-0.0086	0.0033	
856.267	0.0033	-0.0053	0.0020	

Continued on next page

Table A.3 – continued from previous page

f_2 [MHz]	**Point 1** [MHz]	**Point 2** [MHz]	**Point 3** [MHz]	k
863.715	0.0039	-0.0063	0.0024	
865.537	0.0041	-0.0067	0.0026	
875.664	0.0038	-0.0062	0.0024	
880.558	0.0023	-0.0037	0.0014	
882.421	0.0018	-0.0029	0.0011	
882.908	0.0052	-0.0085	0.0032	
883.669	0.0030	-0.0049	0.0019	
883.782	0.0030	-0.0049	0.0019	
910.897	0.0048	-0.0078	0.0030	
913.564	0.0049	-0.0080	0.0031	
927.590	-0.0076	0.0123	-0.0047	
928.747▲	0.0156	-0.0253	0.0097	
931.478	0.0020	-0.0033	0.0012	
937.087	0.0072	-0.0117	0.0045	
937.995	-0.0016	0.0027	-0.0010	
943.779	-0.0003	0.0005	-0.0002	
955.878	-0.0017	0.0027	-0.0010	
958.340	-0.0030	0.0048	-0.0018	
966.667	0.0060	-0.0097	0.0037	
968.775	-0.0037	0.0060	-0.0023	
969.385	-0.0020	0.0032	-0.0012	
978.386	-0.0019	0.0032	-0.0012	
978.523	-0.0016	0.0027	-0.0010	
987.243	0.0011	-0.0018	0.0007	
993.127	-0.0032	0.0051	-0.0020	
995.692	-0.0036	0.0059	-0.0022	
1001.999	-0.0032	0.0052	-0.0020	
1002.804	0.0034	-0.0055	0.0021	
1004.498	0.0038	-0.0061	0.0023	
1007.561	-0.0016	0.0026	-0.0010	
1017.086	0.0045	-0.0072	0.0028	
1020.426	-0.0037	0.0059	-0.0023	
1033.421	0.0029	-0.0048	0.0018	
1035.370	0.0056	-0.0091	0.0035	
1036.424	-0.0015	0.0025	-0.0009	
1052.636	0.0038	-0.0062	0.0024	
1062.290	-0.0026	0.0042	-0.0016	
1070.007	-0.0046	0.0075	-0.0029	
1071.275	-0.0043	0.0070	-0.0027	
1076.646	-0.0045	0.0072	-0.0028	
1079.126	-0.0028	0.0046	-0.0018	
1080.352	0.0013	-0.0022	0.0008	

Continued on next page

Table A.3 – continued from previous page

f_2 [MHz]	**Point 1** [MHz]	**Point 2** [MHz]	**Point 3** [MHz]	k
1081.322	-0.0030	0.0049	-0.0019	
1082.293▲	0.1001	-0.1623	0.0622	
1087.749	-0.0053	0.0086	-0.0033	
1089.655	-0.0075	0.0122	-0.0047	
-	-	-	-	
1095.436	0.0010	-0.0017	0.0006	
1095.914	-0.001	0.0016	-0.0006	
1136.287	-0.0044	0.0072	-0.0028	
1139.274	-0.0039	0.0062	-0.0024	
-	-	-	-	
1150.149	-0.0043	0.0069	-0.0026	
1153.779	-0.0041	0.0066	-0.0025	
1155.963	-0.0047	0.0076	-0.0029	
1163.973	-0.0036	0.0058	-0.0022	
1165.725	-0.0036	0.0058	-0.0022	
1174.816	-0.0043	0.0070	-0.0027	
1177.225	-0.0045	0.0074	-0.0028	
1179.978	-0.0025	0.0041	-0.0016	
1180.639	-0.0033	0.0053	-0.0020	
1184.819	-0.0040	0.0065	-0.0025	
1186.144	-0.0061	0.0098	-0.0038	
1187.664	0.0026	-0.0043	0.0016	
1193.301	-0.0050	0.0080	-0.0031	
1199.700	0.0047	-0.0077	0.0029	
1202.683	-0.0027	0.0044	-0.0017	
1211.298	0.0048	-0.0078	0.0030	
1211.653	-0.0038	0.0061	-0.0023	
1219.691	-0.0058	0.0094	-0.0036	
1222.550	-0.0038	0.0062	-0.0024	
1222.878	-0.0036	0.0059	-0.0023	
1226.228	-0.0042	0.0068	-0.0026	
1242.284	-0.0031	0.0050	-0.0019	
1243.847	-0.0027	0.0044	-0.0017	
1244.202	-0.0036	0.0059	-0.0023	
1254.002	-0.0070	0.0113	-0.0043	
1255.820	0.0023	-0.0037	0.0014	
1259.253	-0.0007	0.0012	-0.0005	
1266.069	-0.0039	0.0063	-0.0024	
1266.863	-0.0044	0.0071	-0.0027	
1271.915▲	0.0129	-0.0209	0.0080	
1272.398	-0.0045	0.0072	-0.0028	
1277.669	-0.0061	0.0099	-0.0038	

Continued on next page

Table A.3 – continued from previous page

f_2 [MHz]	**Point 1** [MHz]	**Point 2** [MHz]	**Point 3** [MHz]	k
1280.991	-0.0052	0.0085	-0.0032	
1281.736	-0.0040	0.0064	-0.0025	
1282.492	-0.0037	0.0060	-0.0023	
1283.555	-0.0036	0.0058	-0.0022	
1286.991	-0.0059	0.0096	-0.0037	
1287.961	-0.0061	0.0098	-0.0038	
1288.643	-0.0034	0.0056	-0.0021	
1289.396	-0.0046	0.0074	-0.0028	
1291.879	-0.0049	0.0080	-0.0031	
1293.126	-0.0074	0.0121	-0.0046	
-	-	-	-	
1297.324▲	-0.0708	0.1147	-0.0439	
1304.660	-0.0042	0.0068	-0.0026	
1305.808	-0.0040	0.0065	-0.0025	